

MoS₂ Quantum Dot/Graphene Hybrids for Advanced Interface Engineering of CH₃NH₃PbI₃ Perovskite Solar Cell with Efficiency over 20%

Leyla Najafi,^{†,‡} Babak Taheri,^{#,‡} Beatriz Martín-García,[†] Sebastiano Bellani,[†] Diego Di Girolamo,[#] Antonio Agresti,[#] Reinier Oropesa-Nuñez,^{†,||} Sara Pescetelli,[#] Luigi Vesce,[#] Emanuele Calabrò,[#] Mirko Prato,[⊥] Antonio E. Del Rio Castillo,[†] Aldo Di Carlo,^{#,£} and Francesco Bonaccorso^{†,||*}*

[†] Graphene Labs, Istituto Italiano di Tecnologia, via Morego 30, 16163 Genova, Italy.

[#] C.H.O.S.E. (Centre for Hybrid and Organic Solar Energy), Department of Electronic Engineering, University of Rome Tor Vergata, Via del Politecnico 1, Rome 00133, Italy.

^{||} BeDimensional Srl., Via Albisola 121, 16163 Genova, Italy.

[⊥] Materials Characterization Facility, Istituto Italiano di Tecnologia, via Morego 30, 16163 Genova, Italy.

[£] L.A.S.E. - Laboratory for Advanced Solar Energy, National University of Science and Technology "MISIS", 119049 Leninskiy prosect 6. Moscow, Russia.

ABSTRACT

Interface engineering of organic-inorganic halide perovskite solar cells (PSCs) plays a pivotal role in achieving high power conversion efficiency (PCE). In fact, perovskite photoactive layer needs to work synergistically with the other functional components of the cell, such as charge transporting/active buffer layers and electrodes. In this context, graphene and related two-dimensional materials (GRMs) are promising candidates to tune “on demand” the interface properties of PSCs. In this work, we fully exploit the potential of GRMs by controlling the optoelectronic properties of hybrids between molybdenum disulfide (MoS_2) and reduced graphene oxide (RGO) as hole transport layer (HTL) and active buffer layer (ABL) in mesoscopic methylammonium lead iodide ($\text{CH}_3\text{NH}_3\text{PbI}_3$) perovskite (MAPbI_3)-based PSC. We show that zero-dimensional MoS_2 quantum dots (MoS_2 QDs), derived by liquid phase exfoliated MoS_2 flakes, provide both hole-extraction and electron-blocking properties. In fact, on the one hand, intrinsic n-type doping-induced intra-band gap states effectively extract the holes through an electron injection mechanism. On the other hand, quantum confinement effects increase the optical band gap of MoS_2 (from 1.4 eV for the flakes to > 3.2 for QDs), raising the minimum energy of its conduction band (from -4.3 eV for the flakes to -2.2 eV for QDs) above the one of conduction band of MAPbI_3 (between -3.7 and -4 eV) and hindering electron collection. The van der Waals hybridization of MoS_2 QDs with functionalized reduced graphene oxide (f-RGO), obtained by chemical silanization-induced linkage between RGO and (3-mercaptopropyl)trimethoxysilane, is effective to homogenize the deposition of HTLs or ABLs onto the perovskite film, since the two-dimensional (2D) nature of RGO effectively plug the pinholes of the MoS_2 QDs films. Our “*graphene interface engineering*” (GIE) strategy based on van der Waals MoS_2 QD/graphene hybrids enable MAPbI_3 -based PSCs to achieve PCE up to 20.12% (average PCE of 18.8%). The possibility to combine quantum and chemical effects into GIE, coupled with the recent success of graphene and GRMs as interfacial layer, represents a promising approach for the development of next-generation PSCs.

INTRODUCTION

Organic-inorganic halide perovskite solar cells (PSCs) are in the spotlight of the photovoltaic (PV) research to rival the leading technologies¹⁻⁴ (*i.e.* crystalline silicon solar cells⁵⁻⁷ and inorganic thin-film solar cells^{8,9}) since power conversion efficiency (PCE) exceeding 20%¹⁰⁻¹² can be obtained by affordable (low-cost and low-temperature) solution processing¹³⁻¹⁵ with scaling-up prospective.¹⁶⁻¹⁹

Methylammonium lead iodide ($\text{CH}_3\text{NH}_3\text{PbI}_3$) perovskite (MAPbI_3) has been intensively studied as light harvesting material from the beginning of the PSC developments^{1,2,20-22} and the elemental composition engineering of its chemistry^{23,24} led to mixed cation and halide PSCs,²⁵ which boosted certified PCE above 22% (*i.e.* 22.1%²⁶ and 22.7%¹⁰). Although the archetypal MAPbI_3 reached certified maximum efficiency of 19.3%²⁷ (uncertified efficiency exceeding 20%²⁸⁻³¹), it still covers a benchmarking role for the optimization and/or validation of PSC architectures³¹⁻³⁴ due to its historical breakthrough in the PV technology over the last years (starting from 2009, PCE of 3.8%²¹).¹⁰ In particular, MAPbI_3 -based PSCs provide a platform to study and design the interface between each functional layers of the PSCs,^{16,35-41} whose carrier transport barrier determines undesirable hysteresis and instabilities effects in PSCs,^{33,42-44} both in mesoscopic^{31,45} and planar structure.⁴⁵ In fact, the photogenerated carriers have to be transported across the interfaces in the PSC structure,^{38,46-48} and charge loss can occurs due to energy barriers and/or interfacial defects.^{38,46-48} Therefore, appropriate energy level tailoring at the interfaces is pivotal in: 1) increasing open circuit voltage (V_{oc}); 2) facilitating charge transfer and extraction,^{49,50} which contribute to increase short circuit current (J_{sc}) and fill factor (FF);^{49,50} 3) eliminating hysteresis phenomena⁵¹⁻⁵³ and 4) extending lifetime^{54,55} of current PSCs. In the run-up to reach the theoretical PCE limit ($\sim 31\%$)⁵⁶ of PSCs (practical limits of 29.5%⁵⁷ and 30.5%⁵⁸ have also been reported by considering intrinsic non-radiative recombination processes), graphene and related two-dimensional (2D) materials (GRMs) are emerging as a paradigm shift of interface engineering to boost the PV performance.^{56,59-73} Actually, the large variety of GRMs offers peculiar (opto)electronic properties^{74,75} that can be on-demand tuned by means of

morphological modification^{76,77} and chemical functionalization.⁷⁸⁻⁸⁰ Moreover, GRMs can be produced from the exfoliation of their bulk counterpart in suitable solvents⁸¹⁻⁸⁵ in form of functional inks,⁸⁶ which can be deposited on different substrates by established large-scale, cost-effective printing/coating techniques,⁸⁷⁻⁹⁰ compatible with solution-based manufacturing of PSCs.^{15,91-93}

With the aim to deeply exploit the use of 2D materials for engineering the interface of PSCs, herein we report a synergistic quantum-chemical approach for controlling the energy band levels and the thin-film morphology of low dimensional, van der Waals hybrids between molybdenum disulfide QDs (MoS₂ QDs) and reduced graphene oxide (RGO) as hole transport layer (HTL) or active buffer layer (ABL) (between HTL and Au electrode) in mesoscopic MAPbI₃-based PSCs (**Figure 1a**). Notably, both 2D MoS₂ and RGO have been previously reported as possible HTLs^{64,72,94-103} or ABL.^{64,104,105} However, their intrinsic work function (WF) (typically < 4.8 eV for both pristine MoS₂¹⁰⁶⁻¹⁰⁹ and RGO¹¹⁰⁻¹¹³) is inferior to that of conventional HTL materials, including 2,2',7,7'-Tetrakis-(N,N-di-4-methoxyphenylamino)-9,9'-spirobifluorene (spiro-OMeTAD) (WF > 4.9,^{114,115} especially for the doped forms mostly exploited as HTLs¹¹⁴⁻¹¹⁷) and poly(3,4-ethylenedioxythiophene):poly(styrene sulfonate) (PEDOT:PSS) (WF ranging between 5.0 and 5.2 eV¹¹⁸⁻¹²¹). This can limit the hole extraction process.^{95,122,123} Moreover, the optical band gap (E_g) of both RGO (< 2 eV,^{124,125} depending on its oxidation level^{124,125}) and MoS₂ (~1.2 eV for bulk,^{126,127} and ~1.8 eV for single-layer¹²⁸⁻¹³⁰) results in minimum energy of conduction band (CB) (~-4.3 eV¹³¹⁻¹³³) lower than that of lowest unoccupied molecular orbital (LUMO) (reported between -4.0¹³⁴⁻¹³⁷ and -3.7 eV^{114,138,139}), not providing electron blocking properties.^{140,141} Therefore, physical/chemical modification of 2D MoS₂ and RGO are needed to tune the optoelectronic properties for their efficient implementation as HTL.^{95,99,110,122,123,142,143} As shown in Figure 1b, zero-dimensional (0D) anodic interlayer of MoS₂ quantum dots (MoS₂ QDs), derived by liquid phase exfoliation (LPE) of MoS₂ flakes,¹⁴⁴ hold optimal electronic structure to effectively extract the photogenerated holes through electron injection mechanism¹⁴⁵⁻¹⁴⁷ from their intrinsic n-type doping¹⁴⁸⁻¹⁵¹-induced intra-band gap states.^{152,153} The latter have been reported to be a consequence of the natural presence in MoS₂ of sulfur vacancies,¹⁵³⁻

¹⁵⁸ impurities^{159,160} and defect.¹⁶¹⁻¹⁶⁴ Quantum confinement effects open the MoS₂ optical bandgap (from 1.4 eV for the flakes to > 3.2 eV for the QDs), raising the minimum energy of the CB of MoS₂ (from -4.3 eV for the flakes to -2.2 eV for the QDs) above the energy of LUMO of MAPbI₃ (between -4.0¹³⁴⁻¹³⁷ and -3.7 eV^{114,138,139}), thus providing electron-blocking properties. Hole-extraction and electron-blocking properties of MoS₂ QDs synergistically suppress the interfacial recombination losses observed in benchmark devices (fluorine doped tin oxide (FTO)/compact TiO₂ (cTiO₂)/mesoporous TiO₂ (mTiO₂)/MAPbI₃/2,2',7,7'-Tetrakis-(N,N-di-4-methoxyphenylamino)-9,9'-spirobifluorene (spiro-OMeTAD)/Au),^{34,165} and in previous cell architectures exploiting native MoS₂ flakes as ABLs.^{64,165} With the aim to form homogeneous (*i.e.* pinhole-free) nm-thick HTLs, MoS₂ QDs, which do not cover totally the MAPbI₃ film after their deposition, are hybridized with chemically (3-mercaptopropyl)trimethoxysilane (MPTS)-functionalized RGO (f-RGO) flakes¹⁶⁶ (the resulting hybrid is herein named MoS₂ QDs:f-RGO).

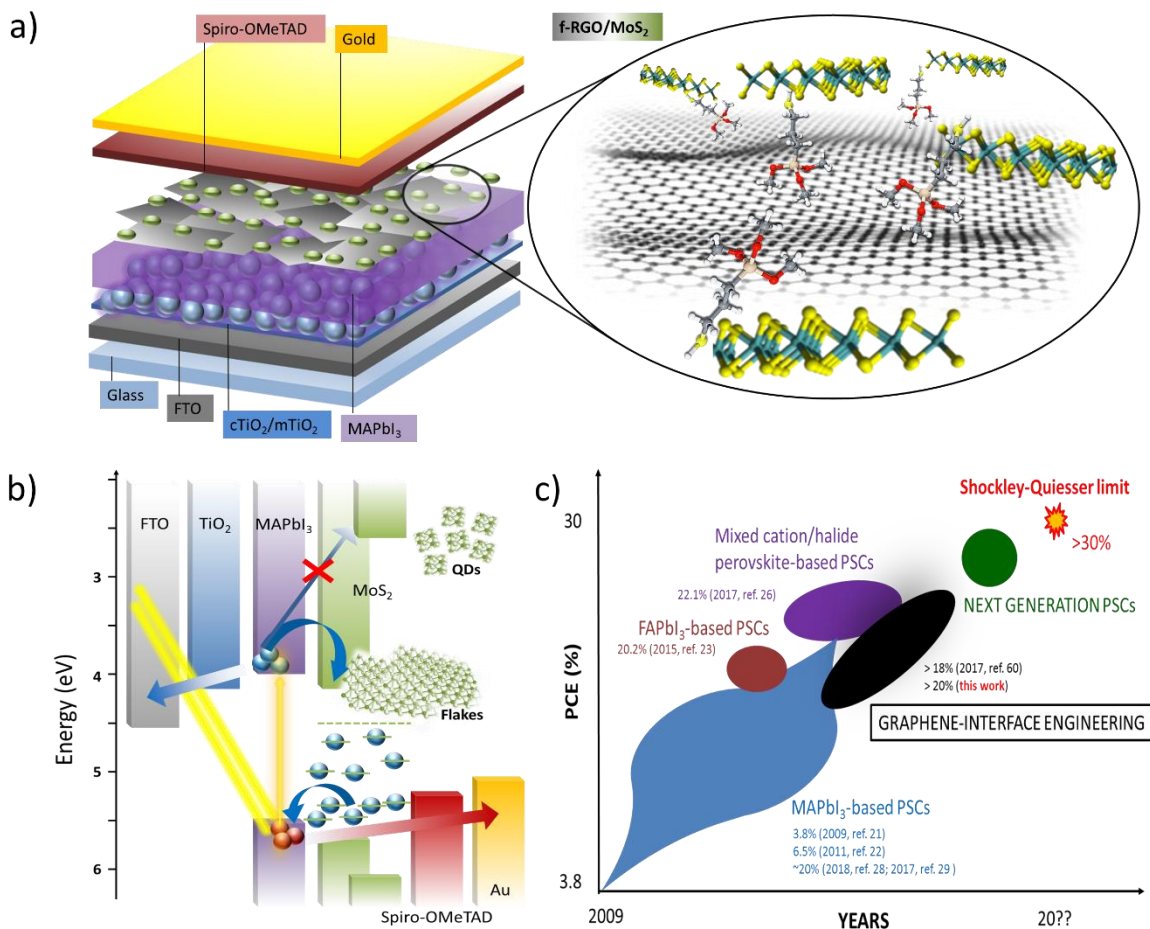


Figure 1. (a) Sketch of mesoscopic MAPbI₃-based PSC exploiting MoS₂ QDs:f-RGO hybrids as both HTL and ABL. (b) Scheme of the energy band edge positions of the materials used in the different components of the assembled mesoscopic MAPbI₃-based PSC. The energy band edge positions of MoS₂ flakes and MoS₂ QDs were determined from OAS and UPS measurements detailed along the text, while those of the other materials were taken from literature: FTO,⁵² TiO₂,⁵² MAPbI₃,¹³⁴⁻¹³⁹ spiro-OMeTAD⁵² and Au⁵². (c) State-of-the-art and predicted PCE evolution for PSCs, highlighting the synergistic potential of GIE and the formulation of advanced perovskite chemistries.

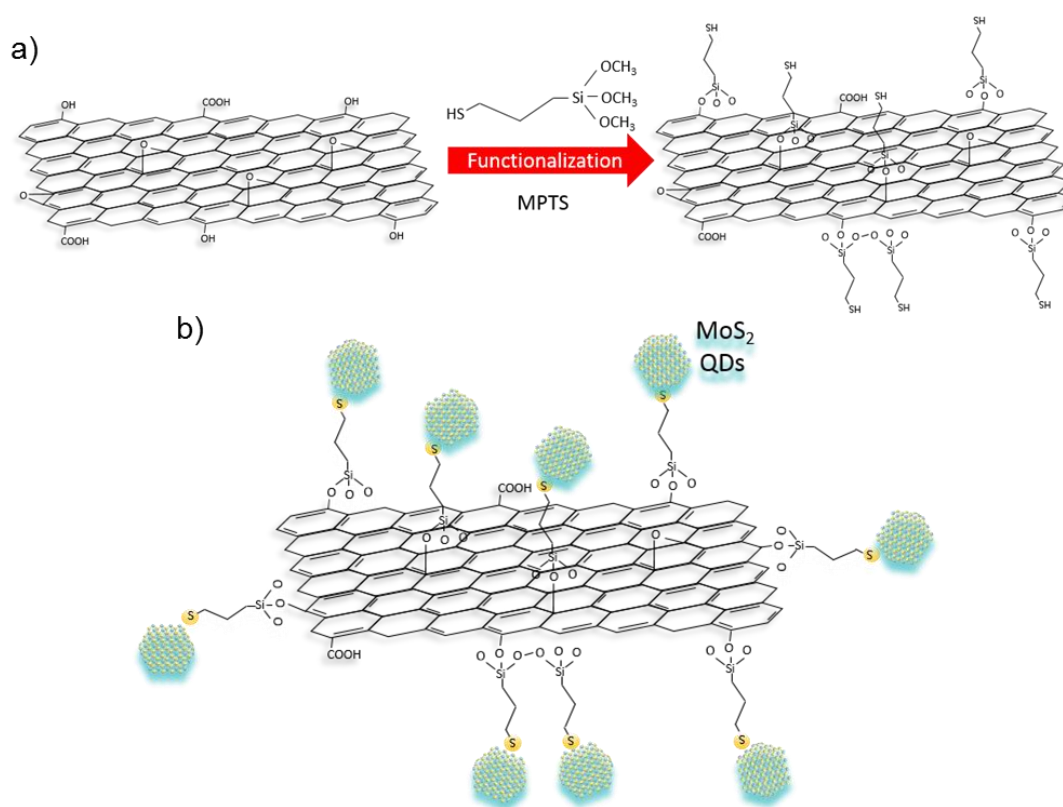
The RGO flakes are effective to plug the pinholes MoS₂ QDs films, thus to homogenize the HTL. The choice of the functionalization for RGO relies on the bifunctional role of MPTS molecules, which effectively anchor onto the RGO flakes (*via* silanization-mediated bonding),^{167,168} while exposed thiol (SH) moieties enable f-RGO to interact with MoS₂ QDs (*via* S-S van der Waals physisorption¹⁶⁹ and/or S-vacancies passivation/filling^{170,171}). Our results show the potential of quantum and chemical effects into “*graphene interface engineering*” (GIE) to produce highly performant MAPbI₃-based PSCs with PCE up to 20.12% (average PCE of 18.8%). The remarkable advances achieved also in the exploitation of graphene flakes- and graphene QDs-doped ETLs, including both mesoscopic TiO₂⁴⁵ and solution-processed SnO₂²⁸, makes GIE a versatile tool for the design of record-high efficiency (solution-processed) next-generation PSCs (Figure 1c).

RESULTS AND DISCUSSION

Production and characterization of MoS₂ QDs, f-RGO and MoS₂ QDs:f-RGO

The MoS₂ QDs were produced through a facile and scalable one-step solvothermal approach starting from MoS₂ flakes previously obtained by LPE of bulk MoS₂ in 2-propanol (IPA),¹⁴⁴ followed by sedimentation-based separation (SBS) process.^{172,173} The LPE process exploits hydrodynamic shear-forces-controlled ultrasonication to overcome the van der Waals forces (15-20 meV Å⁻²,¹⁷⁴ or ~5 meV/atom,^{175,176}) that bind MoS₂ layers.^{81,84,177,178} The SBS process separates various particles on the basis of their sedimentation rate in response to a centrifugal force acting on them.^{84,179} Consequently, MoS₂ flakes were first produced by LPE and subsequently solvothermally treated for the production of MoS₂ QDs.¹⁴⁴ Then, by exploiting SBS we selected MoS₂ QDs, while residuals MoS₂ flakes were discarded as sediment.¹⁴⁴ Reduced graphene oxide was produced by thermal

annealing (1000 °C under a 100 sccm flow of Ar (90%):H₂ (10%)) of graphene oxide (GO)^{180,181} synthesized from graphite flakes using a modified Hummer's method.¹⁸² Subsequently, RGO was functionalized by MPTS *via* silanization-mediated chemical bonding.^{166,183} The silanization process was triggered by the hydrolyzation and condensation of the methoxy groups (–OCH₃) of MPTS, which react with the O moieties of RGO (**Scheme 1a**).^{166,167} A solvent-exchange process^{95,184,185} was carried out to re-disperse MoS₂ QDs and f-RGO dispersions in IPA. The hybrid MoS₂ QDs:f-RGO dispersion was obtained by mixing f-RGO and MoS₂ QDs dispersions with a material weight ratio of 1:2. The hybridization of the materials is completed by the exposed SH moieties of f-RGO, which interact with MoS₂ QDs *via* S-S van der Waals physisorption¹⁶⁹ and/or passivation/filling of the S-vacancies of MoS₂ QDs^{170,171} (**Scheme 1b**).



Scheme 1. Representative sketches of: (a) the functionalization of RGO (structure based on the Lerf-Klinowski model)¹⁸⁶ with MPTS; (b) the hybridization of MoS₂ QDs and f-RGO.

The details of material production and dispersion formulation are reported in Experimental Method section. It is worth noting that the final material dispersions were obtained in low-boiling point

alcohol-based solvents, which are compatible with environmentally friendly, low-temperature and solution-processed deposition methods. By taking advantage of this approach, we exploited spray coating deposition, since it can be applied on irregular surface with higher reproducibility than that obtained with other deposition methods (*e.g.*, spin/blade coating and screen printing).¹⁸⁷ Moreover, with a broader context vision, spray coating is a promising technique to speed up the production of perovskite modules fabrication^{188,189} in view of their market entry.^{190,191}

The lateral size and thickness of the as-produced MoS₂ QDs and f-RGO samples were evaluated by means of transmission electron microscopy (TEM) and atomic force microscopy (AFM), respectively. **Figure 2a,b** show representative TEM and AFM images of MoS₂ QDs. Microscopy statistical analysis of lateral dimension (Figure 2c) and thickness (Figure 2d) shows lognormal distributions peaking at ~2.6 nm and ~1.6 nm, respectively, which means that both one- and few-layer QDs were effectively produced (the monolayer thickness is between 0.7 and 0.8 nm^{128,192}). Notably, the thickness distribution of MoS₂ QDs is similar to that measured for the native MoS₂ flakes (average thickness of ~2.7 nm), whose morphological characterization is reported in the Supporting Information (**Figure S1**). Figure 2e,f report TEM and AFM images of f-RGO flakes, which exhibited irregular shape and rippled paper-like morphology. Microscopy statistical analysis of lateral dimension (Figure 2g) and thickness (Figure 2h) displays lognormal distribution peaked at ~980 nm and ~1.3 nm, respectively. These values are comparable with those obtained for native RGO (average lateral dimension and thickness of 1.7 μm and 1.8 nm, respectively)¹⁸³ (see **Figure S2**). Since the thickness of single-layer pristine graphene is ~0.34 nm,^{193,194} these data indicated that our methodology produced few-layer f-RGO flakes. The structural properties of the materials were investigated by Raman spectroscopy (see SI for Raman spectroscopy analysis additional details, **Figure S3**), confirming their exfoliated crystal structure.

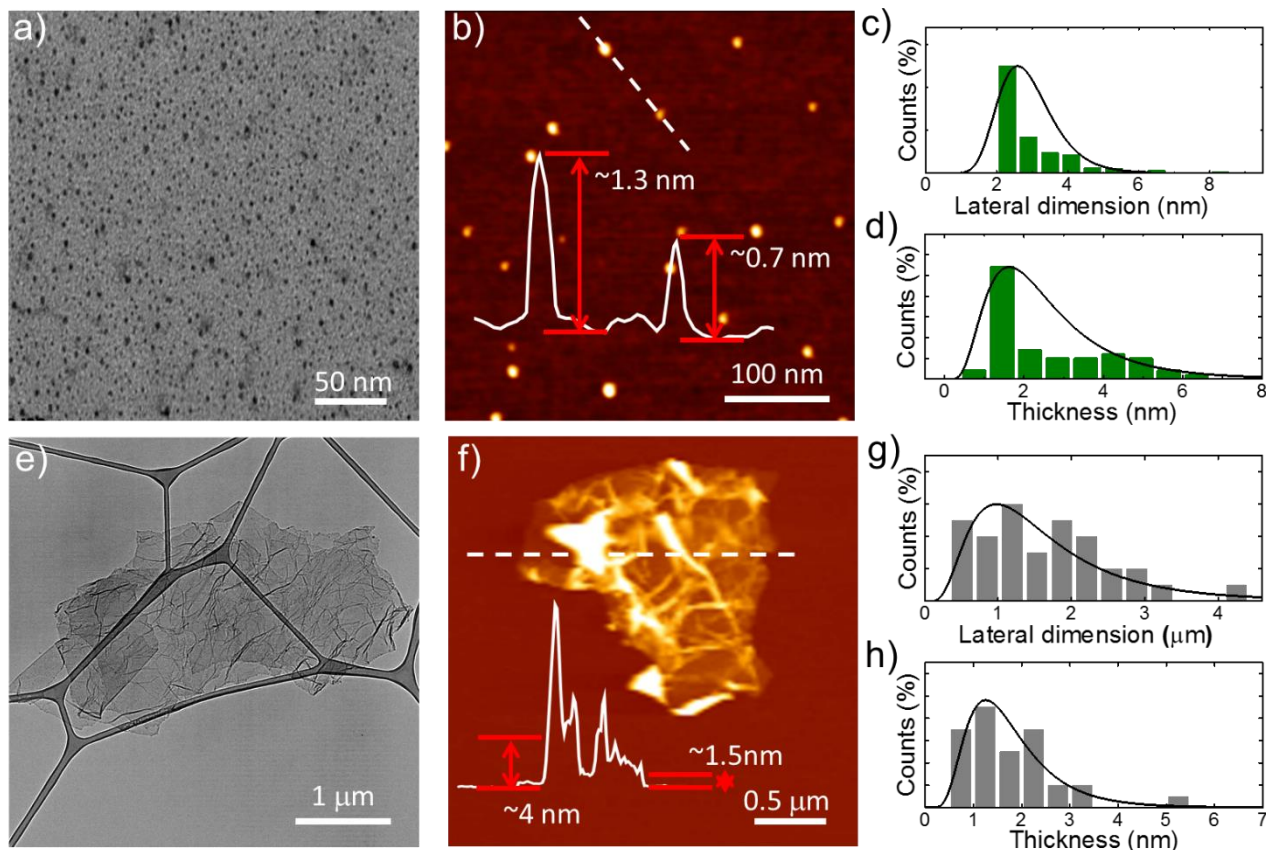


Figure 2. Morphological characterization of (a-d) the as-produced MoS₂ QDs and (e-h) f-RGO flakes. TEM and AFM images of (a, b) MoS₂ QDs and (e, f) f-RGO and the corresponding statistical analysis of (c, g) the lateral dimension and (d, h) the thickness, respectively. The statistical analyses were performed on 50 flakes from the different images collected. Representative height profiles (solid white lines) of the indicated sections (white dashed lines) are also shown in panels (b) and (f).

X-ray photoelectron spectroscopy (XPS) measurements were carried out to determine the elemental composition, chemical phase and interaction of the as-produced MoS₂ QDs:f-RGO samples. **Figure 3a** shows the S 2s and Mo 3d XPS spectra of MoS₂ QDs:f-RGO, together with their deconvolution. The peaks at the lowest binding energy (~ 226 eV and ~ 228 eV) and the peak at ~ 229 eV are assigned to S 2s^{144,195,196} and Mo 3d_{5/2}, respectively, of the semiconducting 2H (trigonal prismatic) phase of MoS₂.^{144,195,196} The peak centered at ~ 232.5 eV can be fitted with two components.^{64,144} The first component (~ 232 eV) is assigned to Mo 3d_{3/2} of the 2H-MoS₂. Instead, the second one (~ 233 eV), as well as the low intensity peak centered at ~ 236 eV, are associated with oxidized phases of Mo,^{177,197} which can be produced during the LPE of bulk MoS₂.^{144,177} However, the percentage content (%c) of oxidized Mo ($< 3\%$) indicates that only a small fraction of the material is oxidized.

Noteworthy, the initial LPE step in IPA can overcome the drawbacks of the LPE of transition metal dichalcogenides^{144,198} (including MoS₂¹⁴⁴) in conventional high-boiling point solvents, such as N-methyl-2-pyrrolidone (NMP)^{64,177,178,199} and N,N-dimethylformamide (DMF),^{64,177,178} where high percentage content (%c) of oxidized species (between 40% and 60%, depending on the process parameter) are typically produced.^{64,177} Moreover, the functionalization process did not cause any additional oxidation of MoS₂ QDs, since the %c of oxidized Mo in the hybrids (< 3%) is also inferior to that of both MoS₂ flakes (< 7%)¹⁴⁴ and MoS₂ QDs (~ 5%)¹⁴⁴. The component at ~228 eV appeared in the S 2s XPS spectrum is ascribed to the presence of SH moieties of f-RGO and proves the interaction of the SH moieties with MoS₂ QDs *via* S-S van der Waals physisorption¹⁶⁹ and/or passivation/filling of the S-vacancies of MoS₂ QDs,^{170,171} as proposed in Scheme 1b. The ratio between %c of Mo 3d and S 2s ascribed to MoS₂ QDs is ~0.5, while for the MoS₂ QDs the same ratio was > 0.5.¹⁴⁴ This confirms that the functionalization process restored the S-vacancies of the native MoS₂ flakes, in agreement with the hybridization mechanism reported in Scheme 1b.

Figure 3b shows the C 1s spectrum of MoS₂ QDs:f-RGO, which is deconvoluted in six components, indicating the C sp² and sp³ network and oxygen functionalities of the f-RGO.²⁰⁰ The C sp² component, centered at 284.5 eV, dominates the spectrum (%c ~75.7%), indicating that the delocalized π -conjugated structure was almost fully restored after the thermal reduction of the native GO (%c of C sp² ~48.5%¹⁸³).^{201,202} Noteworthy, the %c of C sp² in f-RGO is almost the same of that of native RGO (75.6%¹⁸³), indicating that the functionalization process do not alter the basal properties of the RGO flakes.¹⁸³ The component peaking at ~286.9 eV is assigned to C-O bonds (%c = 6.9%). A residue of C sp³ is still present (peak centered at 284.7 eV, %c ~7.6%) as well as carboxylate carbon O-C=O bonds (peak centered at 287.7 eV, %c ~1%). The component observed at ~290.7 eV (%c ~3.7%) is attributed to π - π^* satellite structure (extended delocalized electrons),^{203,204} a characteristic of aromatic C structure. The component peaking at 284.0 eV is also significantly present (%c ~14%). This band can arise as a consequence of C lattice vacancies/distortions introduced mainly during the GO reduction process¹⁸³ and/or the hybridization

of f-RGO with MoS₂ QDs. Regarding the MPTS functionalization of the RGO, Figure 3c shows the Si 2s and S 2p XPS spectra, together with their deconvolution. The appearance of the silane and SH-doublet components peaking at ~153.5 eV and ~163.4 eV, respectively,^{166,205} are fingerprints of the MPTS. The components peaking at ~168.4 eV and ~169.7 eV are attributed to S 2p doublet of SO₄²⁻.^{166,206} These oxidized species are due to both MPTS interacting with O moieties on RGO flakes^{167,207} and MPTS oxidized during the functionalization process. The %c of the oxidized groups is ~5% of the total S content. The ratio between the sum of the %c of SH free and S-S bonds related to the MPTS and that of C bonds on f-RGO is 3%, and estimate the percentage extent of the functionalization of RGO with MPTS.¹⁸³ The interaction between the MPTS and the RGO flakes was confirmed by complementary Fourier-transform infrared (FTIR) measurements. After RGO functionalization, in the f-RGO FTIR spectrum (see SI, **Figure S4**), the Si-O-Si stretching band appears at 1078 cm⁻¹ shifted and broaden compared to pure MPTS (1089 cm⁻¹), indicating the coupling between the alkoxy silane groups and the oxygen groups of RGO, as proposed in Scheme 1. Even more, Si-O-Si band was still present in MoS₂ QDs:f-RGO keeping the same position. This indicated that no modification occurs in the silane-RGO interaction path, leaving only the SH groups as linker option for the MoS₂ QDs (see SI for further discussion). The effectiveness of the MPTS functionalization was also macroscopically observed by noting the improved dispersibility of f-RGO in ethanol compared to that of RGO (**Figure S5**). In fact, MPTS are polar molecules able to decrease the surface energy of native RGO in alcohol-based solvents (~46.1 mN m⁻¹ in ethanol),^{208,209} enhancing dispersion stability and hindering formation of aggregates during films deposition.¹⁸³ In addition, XPS analysis also evidences that S 2p doublet related to S-S bonds (centered at ~164.5 eV) create an interconnection between the MPTS molecules and MoS₂ QDs, since the corresponding %c increases from 10% of the total S content in f-RGO^{167,205} to ~21% of the total S content in MoS₂ QDs-f-RGO.

Optical absorption spectroscopy (OAS) and ultraviolet photoelectron spectroscopy (UPS) measurements were carried out in order to assess the charge-extraction/blocking capability of MoS₂ QDs. Native MoS₂ flakes were also measured for comparison, since they have been previously

reported as effective ABL between MAPbI₃ and spiro-OMeTAD in mesoscopic PSCs.⁶⁴ The UV-Vis absorption spectrum of MoS₂ flakes (Figure 3d) shows peaks at ~670 nm and ~620 nm, which arise from the excitonic transitions between the split valance bands and the minima of the conduction band at the *K*-point of the Brillouin zone of layered MoS₂,^{210,211} known as the A and B, respectively. More in detail, the spin-orbit interaction and interlayer coupling are responsible for the valence band (VB) splitting. The energy difference between the A and B is ~180 meV, which agrees with the values predicted by density functional theory (DFT) calculations (146 meV and 174 meV for monolayer and bilayer, respectively).²¹² The broad absorption band centered at ~400 nm arises from the C and D inter-band transitions between the density of state peaks in the valence and conduction bands.^{213,214} Differently, MoS₂ QDs do not show the absorption peaks of MoS₂ flakes, and their absorption edge shifts toward lower wavelength compared to the latter. This is a consequence of quantum 0D-confinement,^{215,216} which affects the optical properties of nanostructures when their size is comparable or smaller than the excitonic Bohr radius (~23 nm for MoS₂).²¹⁷ Quantum confinement, as well as edge effects, endow excitation-dependent photoluminescence (PL) properties in MoS₂ QDs, (**Figure S6**).^{144,215,218,219} In fact, the PL emission peak of MoS₂ QDs was red-shifted with increasing excitation wavelength.¹⁴⁴ In order to further confirm the effect of quantum confinement on the optical properties of MoS₂, the E_g was evaluated by the $(\alpha hv)^n$ vs. hv (Tauc plot) analysis (Figure 3e) using the Tauc relation $Ahv = Y(hv-E_g)^n$, where A is the absorbance, h is the Planck's constant, v is the photon's frequency, and Y is a proportionality constant.²²⁰ The value of the exponent denotes the nature of the electronic transition, discriminating between direct-allowed transition ($n = 2$) or indirect-allowed transition ($n = 0.5$).²²¹ Bulk MoS₂ is an indirect bandgap semiconductor with $E_g = 1.29$ eV.²²² With decreasing thickness, theoretical^{223,224} and experimental¹²⁸ studies revealed a progressive confinement-induced shift in the indirect bandgap from the bulk value of 1.29 eV up to 1.90 eV, while the direct bandgap increases by only 0.1 eV.¹²⁸ As a consequence of these different scaling properties, MoS₂ undergoes a crossover from an indirect bandgap semiconductor to a direct bandgap material in the monolayer limit.^{128,223,224} The indirect-to-direct bandgap transition has a

strong impact on the PL emission, which shows a dramatic enhancement (by more than a factor of 1000) compared to the one of the bulk counterpart.²²⁵ In the case of our MoS₂ flakes, PL was not detected, in agreement with a dominant few-layer nature evidenced by the AFM statistical analysis of the thickness (Figure 2h). Consequently, in Tauc analysis n was set equal to 0.5 (indirect-allowed transition). Differently, MoS₂ QDs, although show similar thickness of the MoS₂ flakes (see Figure 2d,h), display remarkably PL, since additional quantum effects arising from 0D-confinement activate direct bandgap behavior,^{215,216,217} as proved by PL emission (Figure S6). Then, in Tauc analysis n was set equal to 2 (direct-allowed transition). It is worth noting that n undergoes a size (*i.e.* thickness and lateral dimension)-dependent transition from 2 in direct-bandgap bulk semiconductors to 1 in direct-bandgap nanocrystal.²²⁶ Consequently, the calculated E_g value of MoS₂ QDs has to be considered qualitatively. Taking into account these consideration, the estimated E_g increase from ~ 1.4 eV for MoS₂ flakes to ~ 4.0 eV (~ 3.2 eV assuming $n = 1$, **Figure S7**) for MoS₂ QDs, in agreement with previous studies.²²⁷

Ultraviolet photoelectron spectroscopy measurements allowed the energy Fermi level (E_F), *i.e.* the WF, and VB to be determined. Figure 3f shows that secondary electron cut-off (threshold) energies of the He-I (21.22 eV) UPS spectra is the same for MoS₂ flakes and QDs (~ 16.8 eV), corresponding to a WF of ~ 4.6 eV. The inset to Figure 3f shows the UPS spectra region near the E_F , which allows the maximum energy of VB to be estimated at ~ -5.7 eV for MoS₂ flakes and ~ -6.2 eV for MoS₂ QDs. Taking into account the E_g values estimated by Tauc analysis, the minimum energy of conduction band (CB) is estimated at ~ -4.3 for MoS₂ flakes and ~ -2.2 eV for MoS₂ QDs. The results indicate that, differently from MoS₂ flakes, MoS₂ QDs have minimum energy of CB lower than that of LUMO of MAPbI₃ (between -4.0 ¹³⁴⁻¹³⁷ and -3.7 eV^{114,138,139}). Consequently, MoS₂ QDs effectively act as electron blocking material into the PSC structures (see Figure 1b). Furthermore, the UPS data revealed that both MoS₂ flakes and QDs cannot collect hole from their VB, since the corresponding energy levels (~ -5.7 eV for MoS₂ flakes and ~ -6.2 eV for MoS₂ QDs) are inferior to the one of MAPbI₃ (~ -5.4 eV¹³⁷⁻¹³⁹). Since MoS₂ flakes have been previously reported as HTL material,^{64,72,94-}

⁹⁹ the holes can be extracted from the MAPbI₃ by injecting electrons¹⁴⁵⁻¹⁴⁷ from inter-gap states of MoS₂.^{152,153} The latter have been reported to be a consequence of the intrinsic presence in MoS₂ of S-vacancies¹⁵³⁻¹⁵⁸, impurities^{159,160} and defects.¹⁶¹⁻¹⁶⁴ The presence of these inter-gap states is confirmed by UPS data, which reveal an intrinsic n-type doping of MoS₂ flakes (E_F is just 0.3 eV inferior to the energy of energy minimum of CB, and 1.1 eV superior to the energy maximum of VB). This observation is also in agreement with previous studies,¹⁴⁸⁻¹⁵¹ which evidenced n-type-doping transport measurements in MoS₂-based field effect transistor.¹⁴⁸⁻¹⁵¹ Since XPS analysis revealed equal stoichiometry between MoS₂ flakes and MoS₂ QDs, the hole extraction mechanism deduced for MoS₂ flakes can also be valid for MoS₂ QDs.¹⁴⁴ We also point out that a similar hole-extraction mechanism has been reported for MoO₃ anodic interlayer,^{146,147,228} due to inherent n-type behavior that allows the material to act as donors in transparent conducting oxides.²²⁹

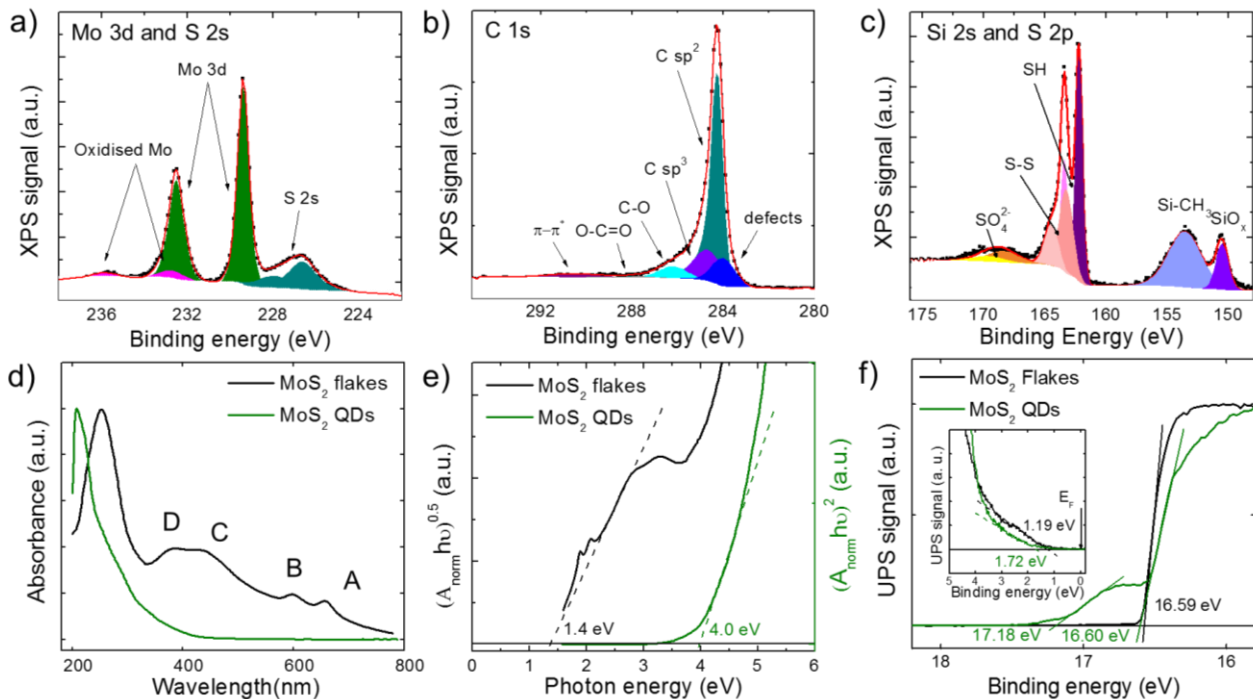


Figure 3. (a) Mo 3d and S 2s, (b) C 1s and (c) Si 2s and S 2p XPS spectra for MoS₂ QDs:f-RGO. The deconvolution of the corresponding XPS spectra is also shown. (d) Absorption spectra of MoS₂ flakes and QDs. (e) Tauc plots of MoS₂ flakes and QDs. (f) Secondary electron threshold region of He-I UPS spectra of MoS₂ flakes and QDs, which were used for estimating the WF values. The inset shows VB region of He-I UPS spectra of MoS₂ flakes and QDs which were used for estimating E_F values.

Perovskite solar cell architecture and their characterization

The optoelectronic characterization of MoS₂ QDs evidenced that they hold both hole-extraction and electron blocking properties, which are the most important requirements for application as HTL.^{41,40,230} In order to deposit continuous and homogeneous film based on MoS₂ QDs, the latter were hybridized with f-RGO flakes, whose 2D nature spontaneously plugs the pinholes in MoS₂ QD films. With the aim to prove the effectiveness of MoS₂ QDs or MoS₂ QDs:f-RGO as hole transport materials, both of them were incorporated into mesoscopic MAPbI₃-based PSCs to be used as HTL or ABL between MAPbI₃ and spiro-OMeTAD. The investigated PSC has the following architecture FTO/cTiO₂/mTiO₂/MAPbI₃/ABL (MoS₂ QDs or f-RGO or MoS₂ QDs:f-RGO)/spiro-OMeTAD/Au. The ABL were also tested as HTL in absence of spiro-OMeTAD. Additional details of the device fabrication are reported in Experimental Methods. It is important to note that MoS₂ QDs and MoS₂ QDs:f-RGO nm-thick films were deposited onto MAPbI₃ films by spray coating the respective dispersions in IPA. The compatibility of the IPA with the MAPbI₃ layer was assessed in previous experiments.^{64,231} A representative FTO/cTiO₂/mTiO₂/MAPbI₃/MoS₂ QDs:f-RGO/spiro-OMeTAD/Au architecture was characterized by cross-sectional scanning electron microscopy (SEM) (**Figure 4a**). The MoS₂ QDs:f-RGO layer is not resolved because of its nm-scale thickness. However, top-view SEM analysis (Figure 4b,c) of MAPbI₃ surface shows that the contrast between different MAPbI₃ grains is reduced after the deposition of ultrathin layer of MoS₂ QDs:f-RGO. This indicates the presence of a nm-thick film of MoS₂ QDs:f-RGO covering MAPbI₃. In addition, SEM/elemental analysis by energy-dispersive X-ray spectroscopy (EDX) were performed on the different MAPbI₃-based PSCs (**Figure S8**), focusing on Pb (M, 2.34 keV), Mo (L α , 2.29 keV) and C (K α , 0.28 keV) peak signal, to evaluate the coverage of the MAPbI₃ surface with MoS₂ QDs and f-RGO. After the deposition of the MoS₂ QDs:f-RGO, a significant increase of the C signal relative to Pb was observed (C/(Pb+Mo) atomic ratio = 15 \pm 2) compared to the reference device (without spiro-OMeTAD, C/Pb atomic ratio = 2.2 \pm 0.1). This further confirms the coverage of the MAPbI₃ surface by the MoS₂ QDs:f-RGO film. Similar results were also evidenced by using only f-RGO (C/Pb atomic ratio = 16 \pm 2).

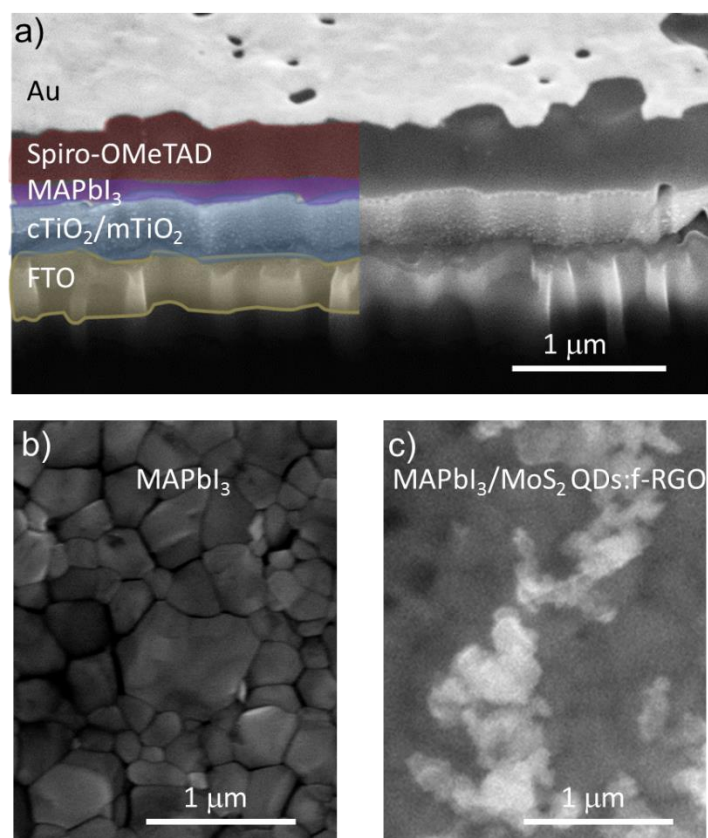


Figure 4. Morphological SEM characterization of PSCs. (a) Cross-sectional SEM image of a representative FTO/cTiO₂/mTiO₂/MAPbI₃/MoS₂ QDs:f-RGO/spiro-OMeTAD/Au architecture. Top-view SEM images of (b) MaPbI₃ surface and (c) MoS₂ QDs:f-RGO film deposited onto MAPbI₃ layer.

The capability of MoS₂ QDs-, f-RGO- and MoS₂ QDs:f-RGO-based ABLs to effectively collect the photogenerated holes was proved by measuring the PV performance of PSCs without spiro-OMeTAD. The current-voltage (I-V) characteristics (**Figure 5a**) show that the best performances are obtained for PSCs adopting MoS₂ QDs:f-RGO as HTL. Such PSCs exhibited a significant increase of PCE compared to the ones without HTL (7.60% vs. 3.01%). Also MoS₂ QDs and f-RGO individually enhanced the PV performance of the HTL-free reference. In particular, MoS₂ QDs increased the J_{sc} of the HTL-free reference from 10.33 mA cm⁻² to 15.52 mA cm⁻², while f-RGO boosted the V_{oc} of the HTL-free reference from 0.69 V to 0.81 V. The poor V_{oc} obtained by the MoS₂ QDs is ascribed to a current leakage in absence of complete coverage of the MAPbI₃ surface, leading to charge recombination at the MAPbI₃/Au interface, since the metallic behavior of Au is not hole-selective.^{232,233} This drawback can be overcome by hybridizing MoS₂ QDs with f-RGO, whose planar nature can provide an effective coverage of the MAPbI₃. These data indicate that the individual

components of MoS₂ QDs:f-RGO synergistically improve the PV performance of the cells. Although the measured PV performance are still lower compared to PSC based on conventional HTLs, these results are promising for the development of viable alternative HTLs based on GRMs.

After these preliminary tests, MoS₂ QDs, f-RGO and MoS₂ QDs:f-RGO were tested as ABL between MAPbI₃ and spiro-OMeTAD. As shown by the I-V curves of representative PSCs in Figure 5b, the PV performance increased with the addition of f-RGO and MoS₂ QDs:f-RGO as ABLs compared to the reference device. The “champion cell” using MoS₂ QDs:f-RGO reached a maximum PCE of 20.12%, a V_{oc} of 1.11 V, a J_{sc} of 22.81 mA cm⁻², and a FF of 79.75%. The reference device has shown a PCE of 16.85%, with a V_{oc} 1.07 V, a J_{sc} of 20.28 mA cm⁻², and a FF of 76.9%. The device using only the MoS₂ QDs as ABL reached PCE of only 14.40%, thus without improving the PV performance of the reference one. The incorporation of f-RGO remarkably increases the J_{sc} of the reference device up to 22.76 mA cm⁻², reaching a PCE of 18.64%. The enhanced J_{sc} of the PSCs exploiting f-RGO and MoS₂ QDs:f-RGO compared to the value obtained by both the reference device and the one based on MoS₂ QDs as ABL is attributed to the efficient charge collection in presence of f-RGO and MoS₂ QDs:f-RGO, respectively. Notably, the optical absorption of the MoS₂ QDs:f-RGO-based PSCs does not show significant differences compared to that of MoS₂ QDs-based PSC, showing an increase of only ~3% and ~8% compared to f-RGO-based and reference PSCs, respectively (**Figure S9**). Hysteresis phenomena, such as anomalous dependence on the voltage scan direction/rate/range,^{43,234} voltage conditioning history,²³⁵ and device configuration,³⁶ could affect the I-V measurements.^{236,237} In order to exclude such effects, the PCE over time at the maximum power point (MPP) was measured for a different batch of cells (**Figure S10**), confirming that the MoS₂ QDs:f-RGO improves the PSC performance of the reference PSC. Forward and reverse I-V curves were also collected (see comparative results of the different ABLs tested SI, **Figure S11**), showing that the presence of MoS₂ QDs:f-RGO as ABLs decreases the hysteresis phenomena compared to

those of the other investigated PSCs, including the reference device adopting spiro-OMeTAD as HTL without ABL.

Steady-state PL measurements were performed to evaluate the capability of the ABLs to extract the photogenerated holes from the MAPbI₃. In fact, the hole-extraction process hinders the radiative charge recombination in the absorber material,²³⁸⁻²⁴⁰ which then show a PL quenching.^{241,242} Figure 5c shows that the addition of ABL between MAPbI₃ and spiro-OMeTAD suppressed the PL emission of MAPbI₃. Quantitatively, the PL decreased by 49.5%, 51.9% and 65.8% in presence of f-RGO, MoS₂ QDs, and MoS₂ QDs:f-RGO, respectively. This means that the ABLs accelerated the hole-extraction dynamics at the photoelectrode.^{239,243} However, I-V measurements clearly show the need of f-RGO to increase the J_{sc} indicating that other effects, such as the morphology of the ABL films, practically influence the PV performance of the PSCs. Incident power conversion efficiency (IPCE) measurements (Figure 5d) are consistent with the I-V ones. In fact, they show that f-RGO and MoS₂ QDs-f-RGO increased the IPCE in the 350-750 nm range by ~5% and ~7% compared to the one of the reference device and the MoS₂ QDs-based PSCs, respectively. The trend of integrated current density (J_{IPCE}) values calculated from IPCE data in the 300-850 nm range at AM1.5G condition (J_{IPCE}(MoS₂ QDs:f-RGO) > J_{IPCE}(f-RGO) > J_{IPCE}(Ref.) > J_{IPCE}(MoS₂ QDs)) are in agreement with the J_{sc} of the different PSCs extrapolated by the corresponding I-V curves. The improvement of V_{oc} and FF compared to the PSCs without spiro-OMeTAD is attributed to both the high WF values of the spiro-OMeTAD compared to those of ABLs, which assist the hole-extraction, and the suppression of the contact between MAPbI₃ and Au, where charge recombination and/or chemical degradation of MAPbI₃ can occur.²⁴⁴

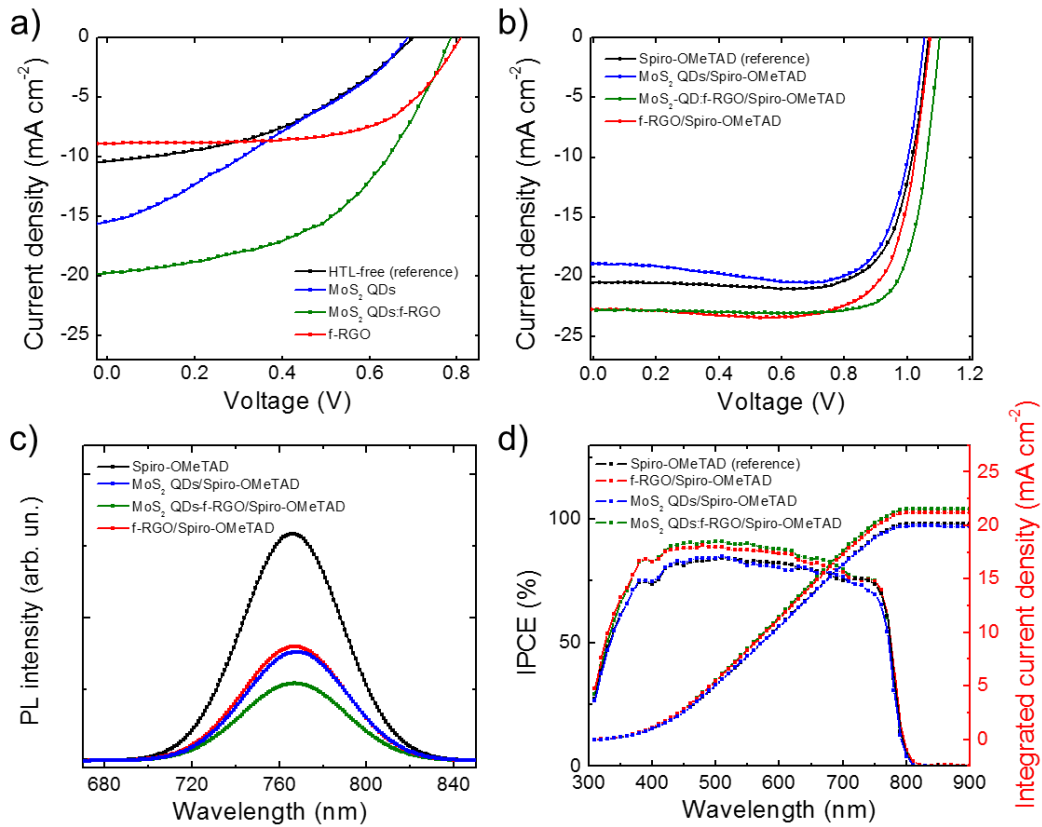


Figure 5. (a,b) I-V characteristics of tested PSCs using MoS₂ QDs, f-RGO and MoS₂ QDs:f-RGO as HTL (panel a) or ABL between MAPbI₃ and spiro OMeTAD. The data for HTL-free and ABL-free devices are shown as references. (c) Steady-state PL measurements of the MAPbI₃ after deposition of spiro-OMeTAD and ABL/spiro-OMeTAD. (d) Incident power conversion efficiency measurements of the various PSCs. The integrated current density of the curves is also shown on the right y-axis (red color).

The statistical PV Figures of Merit (FoM) measured for each set of PSCs using spiro-OMeTAD as HTL and MoS₂ QDs, f-RGO and MoS₂ QDs:f-RGO as ABLs are reported in **Figure 6**, in comparison with those obtained for ABL-free PSC (Ref.). **Table 1** summarizes the PV FoM extracted by the I-V curves of the PSCs shown in Figure 6. These results demonstrate the reproducibility of the PV performance of the PSC incorporating the ABLs. In particular, PSCs using MoS₂ QDs:f-RGO exhibited average PCE value of $18.86 \pm 0.72\%$, corresponding to an increase of 10.6% compared to the reference device without ABL (average PCE = $17.08 \pm 0.73\%$).

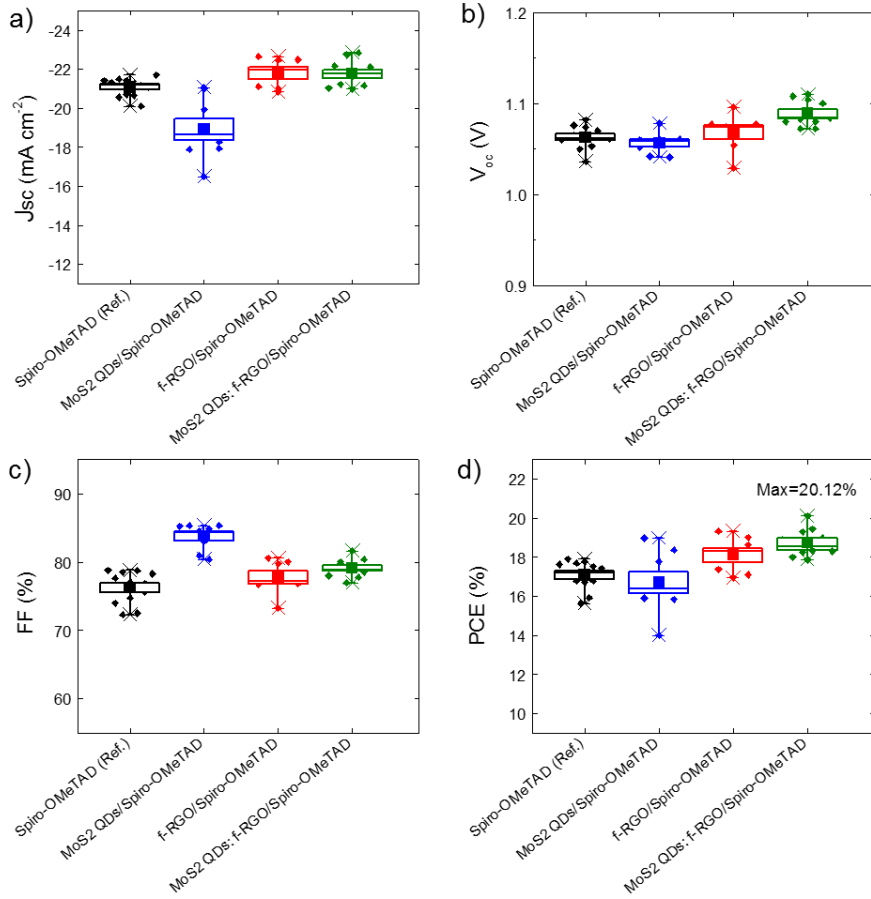


Figure 6. Photovoltaic parameters measured at 1 SUN with the relative standard deviation on 12 PSCs for the four investigated PSCs using spiro-OMeTAD as HTL and MoS₂ QDs, f-RGO and MoS₂ QDs:f-RGO as ABLs: (a) J_{sc}; (b) V_{oc}; (c) FF and (d) PCE. The average values are indicated by square (■).

Table 1. Photovoltaic FOM extracted by the I-V curves of the best performing device of each type of PSCs using spiro-OMeTAD as HTL and MoS₂ QDs, f-RGO and MoS₂ QDs:f-RGO as ABLs. The average PCE of each type of PCS is also shown.

Structure of PSC	V _{oc} [V]	J _{sc} [mA cm ⁻²]	FF [-]	PCE [%]	Average PCE ^[a] [%]
spiro-OMeTAD	1.06	21.49	78.31	17.53	17.08 ± 0.73
MoS ₂ QDs/spiro-OMeTAD	1.06	20.98	83.02	18.98	16.71 ± 1.60
f-RGO/spiro-OMeTAD	1.07	22.49	80.61	19.34	18.11 ± 0.96
MoS ₂ QDs:f-RGO/spiro-OMeTAD	1.11	22.81	79.75	20.12	18.76 ± 0.72

^[a] Average PCE on twelve devices for each type of PSC together with the standard error

In addition to PCE, the long-term stability of PSCs is crucial for real applications.²⁴⁵ Although MAPbI₃ revolutionized the worldwide PV research in the last year, it is intrinsic instable due to its hygroscopicity and tendency to back-convert into its precursors, namely PbI₂ and MAI, during

moisture,²⁴⁶⁻²⁵⁰ oxygen,^{246-248,251-253} and light illumination^{246-248,251,254} exposure. In addition, MAPbI₃ undergoes a phase transition from the tetragonal to cubic phase at ~54 °C,²⁵⁵⁻²⁵⁷ a temperature that can be reached during typical solar cell operation, being not compatible with certification requirement of solar modules (-40–85 °C temperature range).²⁵⁷ This represents the major constraint for the market breakthrough of this technology.^{190,258} So far, the chemical engineering of the perovskite absorber elemental composition has been proved to address the instability issues.^{25,259,260} Device lifetime close to market requirements, *e.g.* 500-hours stability and > 20% PCE, has been recently achieved by formulating perovskites with mixed cations *i.e.* formamidinium (FA), MA and inorganic species (Cs or Ru).^{261,262} One-year stable PSCs were achieved by engineering an ultra-stable 2D/3D (HOOC(CH₂)₄NH₃)₂PbI₄/CH₃NH₃PbI₃ perovskite junction.³⁹ Despite this result, interface engineering of PSCs also affects their stability,^{16,60,61,69,263} since the diffusion of elemental species such as iodine (I) and metal from the electrode materials (*e.g.* Au²⁴⁴ or Ag²⁶⁴) has been recently correlated with the degradation of interfaces and the decay of the PV properties.²⁶⁵ In this context, the incorporation of graphene flakes into mTiO₂ has been demonstrated to increase the chemical stability of overlying MAPbI₃, which exhibited higher crystalline quality compared to the one of MAPbI₃ deposited directly onto mTiO₂⁶⁹ and a freezed tetragonal phase regardless of the temperature.⁶⁹ Active buffer layer based on GRMs improved the charge extraction process compared to that of ABL-free reference, preventing the degradation induced by the diffusion of Au and I.^{71,104,231,266,267} Although it was not the goal of our work to overcome the intrinsic instability of MAPbI₃, the stability of the device after encapsulation was measured in ISOS-D-1 shelf-life aging test protocol²⁶⁸ (**Figure 7**). After 1032 h-aging test, the ABL-based PSCs exhibited a decrease of PCE of only 13.5%, 11.2% and 8.8% for MoS₂ QDs-, f-RGO- and MoS₂ QDs:f-RGO-based PSCs, respectively. These reduction values are significantly lower than the ones shown by the reference PSC without ABL (24.6%).

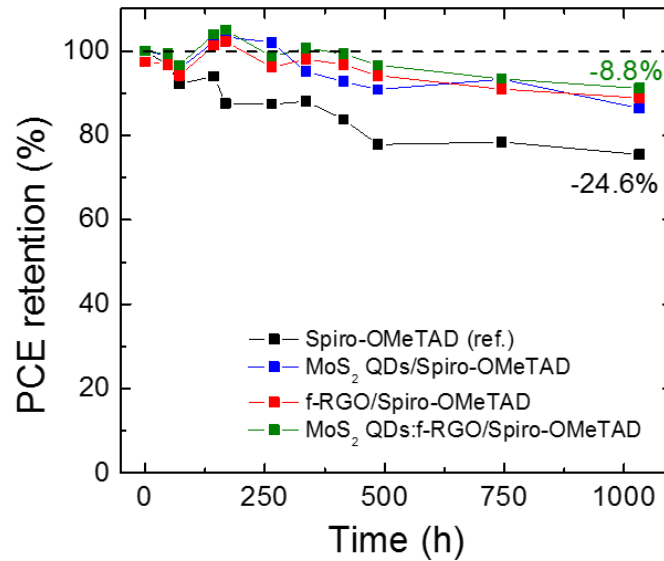


Figure 7. Normalized PCE trends vs. time extracted by I–V characteristics under 1 SUN illumination, periodically acquired during the shelf life test (ISOS-D-1) for the four PSCs.

The improved stability of the ABL-based PSCs compared to the reference PSC is ascribed to the surface passivation of the perovskite layer provided by the ABLs, which mitigate the I migration from the MAPbI₃ into the spiro-OMeTAD²⁶⁹ and the formation of Au pathways from the metal electrode to the MAPbI₃.²⁷⁰

CONCLUSIONS

In conclusion, solution processed low dimensional materials can be designed and combined to improve both efficiency and stability performances of PSCs *via* interface engineering. These results, coupled with the availability of a wide library of 2D materials, demonstrate that GIE is a powerful tool for boosting the PV performance of PSCs. Moreover, 2D materials can be directly produced from cost-effective and environmentally friendly solution-processed methods⁷⁸ from their bulk counterparts,⁸¹⁻⁸⁴ allowing the formulation of inks with on-demand (opto)electronic properties.⁸⁶⁻⁸⁸ Solution processed 2D materials can be deposited on different substrates using established printing/coating techniques,⁸⁷ in order to be integrated as functional layers (*e.g.* charge transport layers and ABLs) into the PSC structures.²⁷¹ By a deep exploitation of the potential offered by 2D materials,^{75,199} we “*ad-hoc*” designed MoS₂ QDs anchored to functional site of RGO flakes to effectively collect the photogenerated holes (as well as blocking electron) from MAPbI₃ towards the

anode contact in mesoscopic MAPbI₃-based PSCs, reaching a maximum PCE values of 20.12% (average PCE of 18.8%). The use of 2D materials is also beneficial for the stability increase of mesoscopic PSCs, indicating the feasibility towards next-generation of PSCs, which exploit both GIE and efficient and stable perovskite chemistries, including mixed cation/halide and 2D perovskites.

EXPERIMENTAL METHODS

Production of materials

Graphene oxide was synthesized from graphite flakes (Sigma Aldrich, +100 mesh $\geq 75\%$ min) using a modified Hummer's method.¹⁸² Briefly, 1 g of graphite and 0.5 g of NaNO₃ (Sigma Aldrich, reagent grade) were mixed, followed by the dropwise addition of 25 mL of H₂SO₄ (Sigma Aldrich). After 4 h, 3 g of KMnO₄ (Alpha Aesar, ACS 99%) was added slowly to the above solution, keeping the temperature at 4 °C with the aid of an ice bath. The mixture was let to react at room temperature overnight and the resulting solution is diluted by adding 2 L of distilled water under vigorous stirring. Finally, the sample was filtered and rinsed with H₂O. Finally the sample was dried at 110 °C overnight.

Reduced graphene oxide was produced by thermal reduction of the as-produced GO^{180,181} in a quartz tube (120 cm length and 25 mm inner diameter) passing through a three zones split furnace (PSC 12/-/600H, Lenton, UK). Experimentally, gas flows were controlled upstream by an array of mass flow controllers (1479A, mks, USA). Under a 100 sccm flow of Ar/H₂ (90/10 %), 100 mg of GO were heated to 100 °C for 20 min to remove the presence of water residuals. Subsequently, a ramp of 20 °C min⁻¹ was used to reach 1000 °C, and stabilized at this temperature for 2 h. Finally, the oven was left to cool to room temperature.

The RGO was functionalized with MPTS, (95%, Sigma Aldrich) in an ethanol (absolute alcohol, $\geq 99.8\%$, without additive, Sigma Aldrich) solution by reflux at 60°C for 15h.¹⁶⁶ For this reaction 250

μL of MPTS were added per mg of RGO. After the synthesis, the silane-functionalized RGO material was recovered by centrifugation (9000 rpm) and re-dispersed in ethanol (EtOH) by vortexing for a second centrifugation (9000 rpm) to remove unreacted silane. A solvent-exchange process^{184,185,95} was carried out to re-disperse the f-RGO in IPA at a concentration of 0.4 mg mL^{-1} .

Molybdenum disulfide quantum dots were produced through a one-step solvothermal method starting from MoS₂ flakes, produced by LPE¹⁴⁴ of bulk MoS₂ crystals in IPA followed by SBS.^{172,173} In detail, 30 mg of MoS₂ bulk crystal (Sigma Aldrich) were added to 50 mL of IPA and then ultrasonicated (Branson® 5800 cleaner, Branson Ultrasonics) for 8 h. The resulting dispersion was ultracentrifuged (Optima™ XE-90 ultracentrifuge, Beckman Coulter) for 15 min at 2700 g, in order to separate the un-exfoliated MoS₂ crystals (collected as sediment) from the thinner MoS₂ flakes that remain in the supernatant. Then, the sample was refluxed in air under stirring for 24 h at 140 °C. The resulting dispersion was subsequently ultracentrifuged for 30 min at 24600 g. Afterward, the supernatant was collected, obtaining the MoS₂ QDs dispersion. By evaporating the solvent, a concentration of 0.2 mg mL^{-1} was obtained.

The hybrid dispersion between MoS₂ QDs and f-RGO were produced by mixing the as-produced component dispersions in a volume ratio of 1:1 (corresponding to a weight ratio of 1:2). By evaporating the solvent, the concentration was doubled in order to have the same amount of the material compared to the native dispersions.

Characterization of materials

Transmission electron microscopy images were taken with a JEM 1011 (JEOL) TEM (thermionic W filament), operating at 100 kV. Morphological and statistical analysis was carried out by using ImageJ® software (NIH) and OriginPro® 9.1 software (OriginLab), respectively. The statistical analysis was performed on 50 flakes from the different TEM images collected. The lateral dimension of each flake was calculated as the maximum Feret's Diameter. Samples for the TEM measurements

were prepared by drop casting the material dispersions onto ultrathin carbon-coated copper grids rinsed with deionized water and subsequently dried under vacuum overnight.

Atomic force microscopy images were taken using a Nanowizard III (JPK Instruments, Germany) mounted onto an Axio Observer D1 (Carl Zeiss, Germany) inverted optical microscope. The AFM measurements were carried out by using PPP-NCHR cantilevers (Nanosensors, USA) with a nominal tip diameter of 10 nm. A drive frequency of ~295 kHz is used. Intermittent contact mode AFM images (512×512 data points) of 2.5×2.5 μm^2 were collected by keeping the working set point above 70% of the free oscillation amplitude. The scan rate for acquisition of images was 0.7 Hz. Height profiles were processed by using the JPK Data Processing software (JPK Instruments, Germany) and the data were analysed with OriginPro[®] 9.1 software. Statistical analysis was carried out by means of Origin 9.1 software on multiple AFM images for each sample, and calculated on 50 flakes. The samples were prepared by drop-casting the materials dispersions onto mica sheets (G250-1, Agar Scientific Ltd., Essex, U.K.) and dried under vacuum.

Optical absorption spectroscopy measurements were carried out on material dispersions by using a Cary Varian 5000 UV–vis spectrometer.

X-ray photoelectron spectroscopy characterization was carried out on a Kratos Axis UltraDLD spectrometer, using a monochromatic Al K α source (15 kV, 20 mA). The spectra were taken on a 300×700 μm^2 area. Wide scans were collected with constant pass energy of 160 eV and energy step of 1 eV. High-resolution spectra were acquired at constant pass energy of 10 eV and energy step of 0.1 eV. The binding energy scale was referenced to the C 1s peak at 284.8 eV. The spectra were analysed using the CasaXPS software (version 2.3.17). The samples were prepared by drop-casting the material dispersions onto Si/SiO₂ substrate (LDB Technologies Ltd) and dried under vacuum.

Fourier-transform infrared spectroscopy was performed in a Bruker Vertex[®] 70v (4000-400 cm⁻¹ range, 100 scans). The samples were prepared by drop casting MPTS, RGO, f-RGO, and MoS₂ QDs:f-RGO films on BaF₂ substrates (IR grade, Crystran[®], IR open window 4000 to 600 cm⁻¹).

Ultraviolet photoelectron spectroscopy analysis was performed to estimate the energy Fermi level (E_F) of the materials under investigation with the same equipment used by XPS, and adopting a He I (21.22 eV) discharge lamp. The E_F was measured from the threshold energy for the emission of secondary electrons during He I excitation. A -9.0 V bias was applied to the sample in order to precisely determine the low kinetic energy cutoff. The samples were prepared by drop-casting onto 50 nm Au-sputter-coated silicon wafers.

Fabrication of solar cells

The solar cells containing four devices were fabricated on laser patterned glass/FTO substrates (Pilkington, $8 \Omega \square^{-1}$), which were washed for 15 min with acetone, ethanol and deionized water in an ultrasonic bath, respectively. Furthermore, a compact 40 nm TiO₂ layer (c-TiO₂) was deposited onto the pre-cleaned laser patterned FTO glass *via* spray pyrolysis (450°C) from a solution consisting of 0.16 M diisopropoxytitanium bis(acetylacetonate) (Ti(AcAc)₂) and 0.4 M acetyl acetone (AcAc) in ethanol. For the mesoporous TiO₂ (m-TiO₂) layer, anatase TiO₂ nanoparticles paste (30NRD, GreatCell SolarDyesol[®]) were dissolved in ethanol by stirring at a w/w ratio of 1:6. Mesoporous layer was deposited onto c-TiO₂ by spin-coating 140 μ L of paste at 3000 rpm for 15 s, and subsequently sintered at 480 °C for 30 min.

Successively, MAPbI₃ perovskite absorber layer was deposited by solvent engineering method. Briefly 717.76 mg mL⁻¹ of PbI₂ and 247.56 mg mL⁻¹ of CH₃NH₃I were dissolved in dimethylformamide:dimethylsulfoxide (DMF:DMSO) 8:1 (v/v) by stirring for 24h at room temperature to obtain the perovskite-based solution. 70 μ L of the perovskite solution was spin coated on the mesoporous layer with two steps spinning, first 1000 rpm for 10 s and then 5000 rpm for 45 s.

Just 34 s before the end of the second spin coating step, 0.7 mL of diethyl ether was dropped on the substrates. Subsequently, the perovskite layer was treated with a double-step annealing process, performed at 50°C for 2 min and then at 100°C for 10 min. After the heat treatment of the perovskite layer, the 2D materials dispersed in IPA were deposited by an automated spray coating equipment (Aurel[®]) onto perovskite layer by using N₂ flow (see SI, for the spray parameter settings, **Figure S12**). 100 µL of HTL material solution containing spiro-OMeTAD (73.5 mg.mL⁻¹, Borun[®] sublimed grade >99.8%) in chlorobenzene (CB, Sigma Aldrich) doped with 26µL of tert-butylpyridine (TBP, Sigma Aldrich, 96%), 16.6 µL of lithium bis(trifluoromethanesulfonyl)imide (Li-TFSI, Sigma Aldrich, 99.95%) of stock solution (520 mg in 1 mL acetonitrile (Sigma Aldrich), and 7.2 µL of cobalt (III) complex solution (FK209 from Lumtec[®]) was deposited by spin coating at 2000 rpm for 20 s. Finally, 80 nm of Au counter electrode was deposited by thermal evaporation in high vacuum condition (10⁻⁶ mbar). For the shelf life tests, the device were encapsulated following the protocol previously reported in ref. 269.

Characterization of solar cells

Scanning electron microscopy analysis of solar cells was performed using a Helios Nanolab[®] 600 DualBeam microscope (FEI Company) and 10kV and 0.2 nA as measurement conditions. For the EDX spectra acquisition and analysis on the solar cells we used the microscope combined with an X-Max detector and INCA[®] system (Oxford Instruments) and 15kV and 0.8 nA as measurement conditions. The samples were imaged without any metal coating or pre-treatment. To evaluate the layered stack of the solar cell by cross section, the samples were prepared using focused ion beam coupled to the microscope.

Current-Voltage (I-V) characteristics of masked and encapsulated devices were acquired in air atmosphere by using a solar simulator (ABET Sun 2000, class A) at AM1.5 and 100 mW cm⁻² illumination conditions, calibrated with a certified reference Si Cell (RERA Solutions RR-1002). Devices were not preconditioned before the I-V measurements. I-V scans were performed by using a

scan rate of 20mV s^{-1} . Incident photon to current conversion efficiency spectra acquisition were carried out by means of a home-made setup composed by a monochromator (Newport, mod. 74000) coupled with a Xe lamp (Oriel Apex, Newport) and a source meter (Keithley, mod. 2612). A home-made LabVIEW program controlled the spectra acquisition.

Shelf-life test was carried out on encapsulated devices (by following the indications of the ISOS-D-1 shelf life ageing test protocol.²⁷² In particular, the devices were kept in the dark, dry conditions (relative humidity < 50%) and at open circuit.

AUTHOR INFORMATION

Corresponding Author

* Tel: +39 01071781795. E-mail: francesco.bonaccorso@iit.it

* Tel: +39 0672597456. E-mail: aldo.dicarlo@uniroma2.it.

Author Contributions

The manuscript was written through contributions of all authors. All authors have given approval to the final version of the manuscript. ‡These authors contributed equally.

Funding Sources

This project has received funding from the European Union's Horizon 2020 research and innovation program under grant agreement no.785219-GrapheneCore2.

ACKNOWLEDGMENT

We thank Electron Microscopy facility – Istituto Italiano di Tecnologia for support in TEM data acquisition; and IIT Clean Room facility and Smart Materials Group for the access to carry out SEM/EDS measurements and FTIR characterization, respectively. ADC gratefully acknowledges

the financial support of the Ministry of Education and Science of the Russian Federation in the framework of Megagrant N° 14.Y26.31.0027.

REFERENCES

- (1) Green, M. A.; Ho-Baillie, A.; Snaith, H. J. The Emergence of Perovskite Solar Cells. *Nat. Photonics* **2014**, *8*, 506.
- (2) Park, N.-G. Perovskite Solar Cells: An Emerging Photovoltaic Technology. *Mater. Today* **2015**, *18*, 65–72.
- (3) Grätzel, M. The Light and Shade of Perovskite Solar Cells. *Nat. Mater.* **2014**, *13*, 838.
- (4) Stranks, S. D.; Snaith, H. J. Metal-Halide Perovskites for Photovoltaic and Light-Emitting Devices. *Nat. Nanotechnol.* **2015**, *10*, 391.
- (5) A., G. M. The Path to 25% Silicon Solar Cell Efficiency: History of Silicon Cell Evolution. *Prog. Photovolt. Res. Appl.* **2009**, *17*, 183–189.
- (6) Masuko, K.; Shigematsu, M.; Hashiguchi, T.; Fujishima, D.; Kai, M.; Yoshimura, N.; Yamaguchi, T.; Ichihashi, Y.; Mishima, T.; Matsubara, N.; Yamanishi, T. Achievement of More Than 25% Conversion Efficiency With Crystalline Silicon Heterojunction Solar Cell. *IEEE J. Photovolt.* **2014**, *4*, 1433–1435.
- (7) Yoshikawa, K.; Kawasaki, H.; Yoshida, W.; Irie, T.; Konishi, K.; Nakano, K.; Uto, T.; Adachi, D.; Kanematsu, M.; Uzu, H.; Yamamoto, K. Silicon Heterojunction Solar Cell with Interdigitated Back Contacts for a Photoconversion Efficiency over 26%. *Nat. Energy* **2017**, *2*, 17032.
- (8) Lee, T. D.; Ebong, A. U. A Review of Thin Film Solar Cell Technologies and Challenges. *Renew. Sustain. Energy Rev.* **2017**, *70*, 1286–1297.
- (9) Shah, A.; Torres, P.; Tscharnner, R.; Wyrsh, N.; Keppner, H. Photovoltaic Technology: The Case for Thin-Film Solar Cells. *Science* **1999**, *285*, 692–698.
- (10) (NREL), T. N. C. for P. (NCPV) at the N. R. E. L. Best Research-Cell Efficiency available from: <https://www.nrel.gov/pv/assets/pdfs/pv-efficiencies-07-17-2018.pdf> (accessed on 05/09/2018)
- (11) Green, M. A.; Ho-Baillie, A. Perovskite Solar Cells: The Birth of a New Era in Photovoltaics. *ACS Energy Lett.* **2017**, *2*, 822–830.
- (12) Chuantian, Z.; J., B. H.; Hongwei, H.; Jinsong, H.; David, C.; Liming, D. Advances in Perovskite Solar Cells. *Adv. Sci.* **2016**, *3*, 1500324.
- (13) Snaith, H. J. Perovskites: The Emergence of a New Era for Low-Cost, High-Efficiency Solar Cells. *J. Phys. Chem. Lett.* **2013**, *4*, 3623–3630.
- (14) Jeon, N. J.; Noh, J. H.; Kim, Y. C.; Yang, W. S.; Ryu, S.; Seok, S. Il. Solvent Engineering for High-Performance Inorganic–organic Hybrid Perovskite Solar Cells. *Nat. Mater.* **2014**, *13*, 897.
- (15) Nie, W.; Tsai, H.; Asadpour, R.; Blancon, J.-C.; Neukirch, A. J.; Gupta, G.; Crochet, J. J.; Chhowalla, M.; Tretiak, S.; Alam, M. A.; Wang, H. L. High-Efficiency Solution-Processed Perovskite Solar Cells with Millimeter-Scale Grains. *Science* **2015**, *347*, 522–525.
- (16) Chen, W.; Wu, Y.; Yue, Y.; Liu, J.; Zhang, W.; Yang, X.; Chen, H.; Bi, E.; Ashraful, I.; Grätzel, M.; Han, L. Efficient and Stable Large-Area Perovskite Solar Cells with Inorganic Charge Extraction Layers. *Science* **2015**, *350*, 944–948.
- (17) Li, X.; Bi, D.; Yi, C.; Decoppet, J.-D.; Luo, J.; Zakeeruddin, S. M.; Hagfeldt, A.; Gratzel, M. A Vacuum Flash-Assisted Solution Process for High-Efficiency Large-Area Perovskite Solar Cells. *Science* **2016**, *353*, 58–62.

- (18) Priyadarshi, A.; Haur, L. J.; Murray, P.; Fu, D.; Kulkarni, S.; Xing, G.; Sum, T. C.; Mathews, N.; Mhaisalkar, S. G. A Large Area (70 cm²) Monolithic Perovskite Solar Module with a High Efficiency and Stability. *Energy Environ. Sci* **2016**, *9*, 3687–3692.
- (19) Hwang, K.; Jung, Y.-S.; Heo, Y.-J.; Scholes, F. H.; Watkins, S. E.; Subbiah, J.; Jones, D. J.; Kim, D.-Y.; Vak, D. Toward Large Scale Roll-to-Roll Production of Fully Printed Perovskite Solar Cells. *Adv. Mater.* **2015**, *27*, 1241–1247.
- (20) Lee, M. M.; Teuscher, J.; Miyasaka, T.; Murakami, T. N.; Snaith, H. J. Efficient Hybrid Solar Cells Based on Meso-Superstructured Organometal Halide Perovskites. *Science* **2012**, *338*, 643–647.
- (21) Kojima, A.; Teshima, K.; Shirai, Y.; Miyasaka, T. Organometal Halide Perovskites as Visible-Light Sensitizers for Photovoltaic Cells. *J. Am. Chem. Soc.* **2009**, *131*, 6050–6051.
- (22) Im, J.-H.; Lee, C.-R.; Lee, J.-W.; Park, S.-W.; Park, N.-G. 6.5% Efficient Perovskite Quantum-Dot-Sensitized Solar Cell. *Nanoscale* **2011**, *3*, 4088–4093.
- (23) Yang, W. S.; Noh, J. H.; Jeon, N. J.; Kim, Y. C.; Ryu, S.; Seo, J.; Seok, S. I. High-Performance Photovoltaic Perovskite Layers Fabricated through Intramolecular Exchange. *Science* **2015**, *348*, 1234–1237.
- (24) Ansari, M. I. H.; Qurashi, A.; Nazeeruddin, M. K. Frontiers, Opportunities, and Challenges in Perovskite Solar Cells: A Critical Review. *J. Photochem. Photobiol. C Photochem. Rev.* **2018**, *35*, 1–24.
- (25) Ono, L. K.; Juarez-Perez, E. J.; Qi, Y. Progress on Perovskite Materials and Solar Cells with Mixed Cations and Halide Anions. *ACS Appl. Mater. Interfaces* **2017**, *9*, 30197–30246.
- (26) Yang, W. S.; Park, B.-W.; Jung, E. H.; Jeon, N. J.; Kim, Y. C.; Lee, D. U.; Shin, S. S.; Seo, J.; Kim, E. K.; Noh, J. H.; Seok, S. I. Iodide Management in Formamidinium-Lead-Halide-based Perovskite Layers for Efficient Solar Cells. *Science* **2017**, *356*, 1376–1379.
- (27) Zhou, H.; Chen, Q.; Li, G.; Luo, S.; Song, T.; Duan, H.-S.; Hong, Z.; You, J.; Liu, Y.; Yang, Y. Interface Engineering of Highly Efficient Perovskite Solar Cells. *Science* **2014**, *345*, 542–546.
- (28) Yang, G.; Chen, C.; Yao, F.; Chen, Z.; Zhang, Q.; Zheng, X.; Ma, J.; Lei, H.; Qin, P.; Xiong, L.; Ke, W. Effective Carrier-Concentration Tuning of SnO₂ Quantum Dot Electron-Selective Layers for High-Performance Planar Perovskite Solar Cells. *Adv. Mater.* **2018**, *30*, 1706023.
- (29) Xie, J.; Huang, K.; Yu, X.; Yang, Z.; Xiao, K.; Qiang, Y.; Zhu, X.; Xu, L.; Wang, P.; Cui, C.; Yang, D. Enhanced Electronic Properties of SnO₂ via Electron Transfer from Graphene Quantum Dots for Efficient Perovskite Solar Cells. *ACS Nano* **2017**, *11*, 9176–9182.
- (30) Zhao, J.; Zheng, X.; Deng, Y.; Li, T.; Shao, Y.; Gruverman, A.; Shield, J.; Huang, J. Is Cu a Stable Electrode Material in Hybrid Perovskite Solar Cells for a 30-Year Lifetime? *Energy Environ. Sci* **2016**, *9*, 3650–3656.
- (31) Shin, S. S.; Yeom, E. J.; Yang, W. S.; Hur, S.; Kim, M. G.; Im, J.; Seo, J.; Noh, J. H.; Seok, S. I. Colloidally Prepared La-Doped BaSnO₃ Electrodes for Efficient, Photostable Perovskite Solar Cells. *Science* **2017**, *356*, 167–171.
- (32) Jun-Yuan, J.; Yi-Fang, C.; Mu-Huan, L.; Shin-Rung, P.; Tzung-Fang, G.; Peter, C.; Ten-Chin, W. CH₃NH₃PbI₃ Perovskite/Fullerene Planar-Heterojunction Hybrid Solar Cells. *Adv. Mater.* **2013**, *25*, 3727–3732.
- (33) Kim, H.-S.; Park, N.-G. Parameters Affecting I–V Hysteresis of CH₃NH₃PbI₃ Perovskite Solar Cells: Effects of Perovskite Crystal Size and Mesoporous TiO₂ Layer. *J. Phys. Chem. Lett.* **2014**, *5*, 2927–2934.
- (34) Bi, D.; Yang, L.; Boschloo, G.; Hagfeldt, A.; Johansson, E. M. J. Effect of Different Hole Transport Materials on Recombination in CH₃NH₃PbI₃ Perovskite-Sensitized Mesoscopic Solar Cells. *J. Phys. Chem. Lett.* **2013**, *4*, 1532–1536.
- (35) Zhao, P.; Kim, B. J.; Jung, H. S. Passivation in Perovskite Solar Cells: A Review. *Mater. Today Energy* **2018**, *7*, 267–286.

- (36) Shao, Y.; Xiao, Z.; Bi, C.; Yuan, Y.; Huang, J. Origin and Elimination of Photocurrent Hysteresis by Fullerene Passivation in CH₃NH₃PbI₃ Planar Heterojunction Solar Cells. *Nat. Commun.* **2014**, *5*, 5784.
- (37) Xing, G.; Mathews, N.; Sun, S.; Lim, S. S.; Lam, Y. M.; Grätzel, M.; Mhaisalkar, S.; Sum, T. C. Long-Range Balanced Electron- and Hole-Transport Lengths in Organic-Inorganic CH₃NH₃PbI₃. *Science* **2013**, *342*, 344–347.
- (38) Yang, G.; Wang, C.; Lei, H.; Zheng, X.; Qin, P.; Xiong, L.; Zhao, X.; Yan, Y.; Fang, G. Interface Engineering in Planar Perovskite Solar Cells: Energy Level Alignment, Perovskite Morphology Control and High Performance Achievement. *J Mater Chem A* **2017**, *5*, 1658–1666.
- (39) Grancini, G.; Roldán-Carmona, C.; Zimmermann, I.; Mosconi, E.; Lee, X.; Martineau, D.; Nabey, S.; Oswald, F.; De Angelis, F.; Graetzel, M.; Nazeeruddin, M. K. One-Year Stable Perovskite Solar Cells by 2D/3D Interface Engineering. *Nat. Commun.* **2017**, *8*, 15684.
- (40) Malinkiewicz, O.; Yella, A.; Lee, Y. H.; Espallargas, G. M.; Graetzel, M.; Nazeeruddin, M. K.; Bolink, H. J. Perovskite Solar Cells Employing Organic Charge-Transport Layers. *Nat. Photonics* **2013**, *8*, 128.
- (41) Grill, I.; Aygüler, M. F.; Bein, T.; Docampo, P.; Hartmann, N. F.; Handloser, M.; Hartschuh, A. Charge Transport Limitations in Perovskite Solar Cells: The Effect of Charge Extraction Layers. *ACS Appl. Mater. Interfaces* **2017**, *9*, 37655–37661.
- (42) Snaith, H. J.; Abate, A.; Ball, J. M.; Eperon, G. E.; Leijtens, T.; Noel, N. K.; Stranks, S. D.; Wang, J. T.-W.; Wojciechowski, K.; Zhang, W. Anomalous Hysteresis in Perovskite Solar Cells. *J. Phys. Chem. Lett.* **2014**, *5*, 1511–1515.
- (43) Unger, E. L.; Hoke, E. T.; Bailie, C. D.; Nguyen, W. H.; Bowering, A. R.; Heumüller, T.; Christoforo, M. G.; McGehee, M. D. Hysteresis and Transient Behavior in Current-Voltage Measurements of Hybrid-Perovskite Absorber Solar Cells. *Energy Environ. Sci* **2014**, *7*, 3690–3698.
- (44) Heo, J. H.; Han, H. J.; Kim, D.; Ahn, T. K.; Im, S. H. Hysteresis-Less Inverted CH₃NH₃PbI₃ Planar Perovskite Hybrid Solar Cells with 18.1% Power Conversion Efficiency. *Energy Environ. Sci* **2015**, *8*, 1602–1608.
- (45) Pascoe, A. R.; Yang, M.; Kopidakis, N.; Zhu, K.; Reese, M. O.; Rumbles, G.; Fekete, M.; Duffy, N. W.; Cheng, Y.-B. Planar *versus* Mesoscopic Perovskite Microstructures: The Influence of CH₃NH₃PbI₃ Morphology on Charge Transport and Recombination Dynamics. *Nano Energy* **2016**, *22*, 439–452.
- (46) Yang, B.; Xiangyue, M.; Shihe, Y. Interface Engineering for Highly Efficient and Stable Planar P-I-N Perovskite Solar Cells. *Adv. Energy Mater.* **2017**, *8*, 1701883.
- (47) Schulz, P.; Edri, E.; Kirmayer, S.; Hodes, G.; Cahen, D.; Kahn, A. Interface Energetics in Organo-Metal Halide Perovskite-Based Photovoltaic Cells. *Energy Environ. Sci.* **2014**, *7*, 1377–1381.
- (48) Sum, T. C.; Chen, S.; Xing, G.; Liu, X.; Wu, B. Energetics and Dynamics in Organic–inorganic Halide Perovskite Photovoltaics and Light Emitters. *Nanotechnology* **2015**, *26*, 342001.
- (49) Azhar, F.; Lukas, S.-M.; Germà, G.-B.; Rajan, J.; Ivan, M.-S. Interfaces in Perovskite Solar Cells. *Adv. Energy Mater.* **2017**, *7* (22), 1700623.
- (50) Schulz, P. Interface Design for Metal Halide Perovskite Solar Cells. *ACS Energy Lett.* **2018**, *3*, 1287–1293.
- (51) Sherkar, T. S.; Momblona, C.; Gil-Escrig, L.; Ávila, J.; Sessolo, M.; Bolink, H. J.; Koster, L. J. A. Recombination in Perovskite Solar Cells: Significance of Grain Boundaries, Interface Traps, and Defect Ions. *ACS Energy Lett.* **2017**, *2*, 1214–1222.
- (52) Pantaler, M.; Cho, K. T.; Queloz, V. I. E.; García Benito, I.; Fettikeyhauer, C.; Anusca, I.; Nazeeruddin, M. K.; Lupascu, D. C.; Grancini, G. Hysteresis-Free Lead-Free Double-Perovskite Solar Cells by Interface Engineering. *ACS Energy Lett.* **2018**, 1781–1786.

- (53) Peng, J.; Wu, Y.; Ye, W.; Jacobs, D. A.; Shen, H.; Fu, X.; Wan, Y.; Duong, T.; Wu, N.; Barugkin, C.; Nguyen, H. T.; Zhong, D. Interface Passivation Using Ultrathin Polymer–fullerene Films for High-Efficiency Perovskite Solar Cells with Negligible Hysteresis. *Energy Environ. Sci.* **2017**, *10*, 1792–1800.
- (54) Lira-Cantú, M. Perovskite Solar Cells: Stability Lies at Interfaces. *Nat. Energy* **2017**, *2*, 17115.
- (55) Christians, J. A.; Schulz, P.; Tinkham, J. S.; Schloemer, T. H.; Harvey, S. P.; Tremolet de Villers, B. J.; Sellinger, A.; Berry, J. J.; Luther, J. M. Tailored Interfaces of Unencapsulated Perovskite Solar Cells for >1,000 Hour Operational Stability. *Nat. Energy* **2018**, *3*, 68–74.
- (56) Sha, W. E. I.; Ren, X.; Chen, L.; Choy, W. C. H. The Efficiency Limit of CH₃NH₃PbI₃ Perovskite Solar Cells. *Appl. Phys. Lett.* **2015**, *106*, 221104.
- (57) Baloch, A. A. B.; Hossain, M. I.; Tabet, N.; Alharbi, F. H. Practical Efficiency Limit of Methylammonium Lead Iodide Perovskite (CH₃NH₃PbI₃) Solar Cells. *J. Phys. Chem. Lett.* **2018**, *9*, 426–434.
- (58) Pazos-Outón, L. M.; Xiao, T. P.; Yablonovitch, E. Fundamental Efficiency Limit of Lead Iodide Perovskite Solar Cells. *J. Phys. Chem. Lett.* **2018**, *9*, 1703–1711.
- (59) Agresti, A.; Pescetelli, S.; Palma, A. L.; Del Rio Castillo, A. E.; Konios, D.; Kakavelakis, G.; Razza, S.; Cinà, L.; Kymakis, E.; Bonaccorso, F.; Di Carlo, A. Graphene Interface Engineering for Perovskite Solar Modules: 12.6% Power Conversion Efficiency over 50 cm² Active Area. *ACS Energy Lett.* **2017**, *2*, 279–287.
- (60) Agresti, A.; Pescetelli, S.; Taheri, B.; Del Rio Castillo, A. E.; Cina, L.; Bonaccorso, F.; Di Carlo, A. Graphene–Perovskite Solar Cells Exceed 18 % Efficiency: A Stability Study. *ChemSusChem* **2016**, *9*, 2609–2619.
- (61) Kakavelakis, G.; Maksudov, T.; Konios, D.; Kioseoglou, G.; Stratakis, E.; Kymakis, E. Efficient and Highly Air Stable Planar Inverted Perovskite Solar Cells with Reduced Graphene Oxide Doped PCBM Electron Transporting Layer. *Adv. Energy Mater.* **2016**, *7*, 1602120.
- (62) Agresti, A.; Pescetelli, S.; Cina, L.; Dimitrios, K.; Kakavelakis, G.; Kymakis, E.; Di Carlo, A. Efficiency and Stability Enhancement in Perovskite Solar Cells by Inserting Lithium-Neutralized Graphene Oxide as Electron Transporting Layer. *Adv. Funct. Mater.* **2016**, *26*, 2686–2694.
- (63) Cho, K. T.; Grancini, G.; Lee, Y.; Konios, D.; Paek, S.; Kymakis, E.; Nazeeruddin, M. K. T. Beneficial Role of Reduced Graphene Oxide for Electron Extraction in Highly Efficient Perovskite Solar Cells. *ChemSusChem* **2016**, *9*, 3040–3044.
- (64) Capasso, A.; Matteocci, F.; Najafi, L.; Prato, M.; Buha, J.; Cinà, L.; Pellegrini, V.; Di Carlo, A.; Bonaccorso, F. Few-Layer MoS₂ Flakes as Active Buffer Layer for Stable Perovskite Solar Cells. *Adv. Energy Mater.* **2016**, *6*, 1600920.
- (65) Shan, C.; Gaoquan, S. Two-Dimensional Materials for Halide Perovskite-Based Optoelectronic Devices. *Adv. Mater.* **2017**, *29*, 1605448.
- (66) Van Le, Q.; Choi, J.-Y.; Kim, S. Y. Recent Advances in the Application of Two-Dimensional Materials as Charge Transport Layers in Organic and Perovskite Solar Cells. *FlatChem* **2017**, *2*, 54–66.
- (67) Chen, W.; Li, K.; Wang, Y.; Feng, X.; Liao, Z.; Su, Q.; Lin, X.; He, Z. Black Phosphorus Quantum Dots for Hole Extraction of Typical Planar Hybrid Perovskite Solar Cells. *J. Phys. Chem. Lett.* **2017**, *8*, 591–598.
- (68) Muduli, S. K.; Varrla, E.; Kulkarni, S. A.; Han, G.; Thirumal, K.; Lev, O.; Mhaisalkar, S.; Mathews, N. 2D Black Phosphorous Nanosheets as a Hole Transporting Material in Perovskite Solar Cells. *J. Power Sources* **2017**, *371*, 156–161.
- (69) Biccari, F.; Gabelloni, F.; Burzi, E.; Gurioli, M.; Pescetelli, S.; Agresti, A.; Del Rio Castillo, A. E.; Ansaldo, A.; Kymakis, E.; Bonaccorso, F.; Di Carlo, A. Graphene-Based Electron

Transport Layers in Perovskite Solar Cells: A Step-Up for an Efficient Carrier Collection. *Adv. Energy Mater.* **2017**, *7*, 1701349.

- (70) Ruina, D.; Yangyang, W.; Jie, W.; Xianyu, D. Metal–Organic-Compound-Modified MoS₂ with Enhanced Solubility for High-Performance Perovskite Solar Cells. *ChemSusChem* **2017**, *10*, 2869–2874.
- (71) Kakvelakis, G.; Paradisanos, I.; Paci, B.; Generosi, A.; Papachatzakis, M.; Maksukov, T.; Najafi, L.; Del Rio Castillo, A. E.; Kioseoglou, G.; Stratakis, E.; Bonaccorso, F.; Kymakis, E. Extending the Continuous Operating Lifetime of Perovskite Solar Cells with a Molybdenum Disulfide Hole Extraction Interlayer. *Adv. Energy Mater.* **2018**, *8*, 1702287.
- (72) Dasgupta, U.; Chatterjee, S.; Pal, A. J. Thin-Film Formation of 2D MoS₂ and Its Application as a Hole-Transport Layer in Planar Perovskite Solar Cells. *Sol. Energy Mater. Sol. Cells* **2017**, *172*, 353–360.
- (73) Kuila, T.; Bose, S.; Mishra, A. K.; Khanra, P.; Kim, N. H.; Lee, J. H. Chemical Functionalization of Graphene and Its Applications. *Prog. Mater. Sci.* **2012**, *57*, 1061–1105.
- (74) Ferrari, A. C.; Bonaccorso, F.; Fal'ko, V.; Novoselov, K. S.; Roche, S.; Bøggild, P.; Borini, S.; Koppens, F. H. L.; Palermo, V.; Pugno, N.; Garrido, J. A.; Sordan R.; Bianco, A.; Ballerini, L.; Prato, M.; Lidorikis, E.; Kivioja, J.; Marinelli, C.; Ryhänen, T.; Morpurgo, A.; *et al.* Science and Technology Roadmap for Graphene, Related Two-Dimensional Crystals, and Hybrid Systems. *Nanoscale* **2015**, *7*, 4598–4810.
- (75) Xiaodong, Z.; Yiyong, M.; Dongqing, W.; Fan, Z.; Xinliang, F. Two-Dimensional Soft Nanomaterials: A Fascinating World of Materials. *Adv. Mater.* **2014**, *27*, 403–427.
- (76) Terrones, M.; Botello-Méndez, A. R.; Campos-Delgado, J.; López-Urías, F.; Vega-Cantú, Y. I.; Rodríguez-Macías, F. J.; Elías, A. L.; Muñoz-Sandoval, E.; Cano-Márquez, A. G.; Charlier, J.-C.; Terrones, H. Graphene and Graphite Nanoribbons: Morphology, Properties, Synthesis, Defects and Applications. *Nano Today* **2010**, *5*, 351–372.
- (77) Jia, X.; Campos-Delgado, J.; Terrones, M.; Meunier, V.; Dresselhaus, M. S. Graphene Edges: A Review of Their Fabrication and Characterization. *Nanoscale* **2011**, *3*, 86–95.
- (78) Samori, P.; Palermo, V.; Feng, X. Chemical Approaches to 2D Materials. *Adv. Mater.* **2016**, *28*, 6027–6029.
- (79) Georgakilas, V.; Otyepka, M.; Bourlinos, A. B.; Chandra, V.; Kim, N.; Kemp, K. C.; Hobza, P.; Zboril, R.; Kim, K. S. Functionalization of Graphene: Covalent and Non-Covalent Approaches, Derivatives and Applications. *Chem. Rev.* **2012**, *112*, 6156–6214.
- (80) Chhowalla, M.; Shin, H. S.; Eda, G.; Li, L.-J.; Loh, K. P.; Zhang, H. The Chemistry of Two-Dimensional Layered Transition Metal Dichalcogenide Nanosheets. *Nat. Chem.* **2013**, *5*, 263.
- (81) Nicolosi, V.; Chhowalla, M.; Kanatzidis, M. G.; Strano, M. S.; Coleman, J. N. Liquid Exfoliation of Layered Materials. *Science* **2013**, *340*, 1226419.
- (82) Ciesielski, A.; Samori, P. Graphene *via* Sonication Assisted Liquid-Phase Exfoliation. *Chem Soc Rev* **2014**, *43*, 381–398.
- (83) Parvez, K.; Yang, S.; Feng, X.; Müllen, K. Exfoliation of Graphene *via* Wet Chemical Routes. *Synth. Met.* **2015**, *210*, 123–132.
- (84) Bonaccorso, F.; Lombardo, A.; Hasan, T.; Sun, Z.; Colombo, L.; Ferrari, A. C. Production and Processing of Graphene and 2d Crystals. *Mater. Today* **2012**, *15*, 564–589.
- (85) Del Rio Castillo, A. E.; Pellegrini, V.; Ansaldo, A.; Ricciardella, F.; Sun, H.; Marasco, L.; Buha, J.; Dang, Z.; Gagliani, L.; Lago, E.; Bonaccorso, F. High-Yield Production of 2D Crystals by Wet-Jet Milling. *Mater. Horiz.* **2018**, *5*, 890–904.
- (86) Bonaccorso, F.; Bartolotta, A.; Coleman, J. N.; Backes, C. 2D-Crystal-Based Functional Inks. *Adv. Mater.* **2016**, *28*, 6136–6166.
- (87) Tung, V. C.; Allen, M. J.; Yang, Y.; Kaner, R. B. High-Throughput Solution Processing of Large-Scale Graphene. *Nat. Nanotechnol.* **2008**, *4*, 25.
- (88) Li, D.; Müller, M. B.; Gilje, S.; Kaner, R. B.; Wallace, G. G. Processable Aqueous Dispersions of Graphene Nanosheets. *Nat. Nanotechnol.* **2008**, *3*, 101.

- (89) Torrisi, F.; Hasan, T.; Wu, W.; Sun, Z.; Lombardo, A.; Kulmala, T. S.; Hsieh, G.-W.; Jung, S.; Bonaccorso, F.; Paul, P. J.; Chu, D. Inkjet-Printed Graphene Electronics. *ACS Nano* **2012**, *6*, 2992–3006.
- (90) Secor, E. B.; Lim, S.; Zhang, H.; Frisbie, C. D.; Francis, L. F.; Hersam, M. C. Gravure Printing of Graphene for Large-Area Flexible Electronics. *Adv. Mater.* **2014**, *26*, 4533–4538.
- (91) You, J.; Hong, Z.; Yang, Y.; Chen, Q.; Cai, M.; Song, T.-B.; Chen, C.-C.; Lu, S.; Liu, Y.; Zhou, H.; Yang, Y. Low-Temperature Solution-Processed Perovskite Solar Cells with High Efficiency and Flexibility. *ACS Nano* **2014**, *8*, 1674–1680.
- (92) Tan, H.; Jain, A.; Voznyy, O.; Lan, X.; García de Arquer, F. P.; Fan, J. Z.; Quintero-Bermudez, R.; Yuan, M.; Zhang, B.; Zhao, Y.; Fan, F. Efficient and Stable Solution-Processed Planar Perovskite Solar Cells via Contact Passivation. *Science* **2017**, *355*, 722–726
- (93) Chueh, C.-C.; Li, C.-Z.; Jen, A. K.-Y. Recent Progress and Perspective in Solution-Processed Interfacial Materials for Efficient and Stable Polymer and Organometal Perovskite Solar Cells. *Energy Environ. Sci.* **2015**, *8*, 1160–1189.
- (94) Singh, E.; Kim, K. S.; Yeom, G. Y.; Nalwa, H. S. Atomically Thin-Layered Molybdenum Disulfide (MoS₂) for Bulk-Heterojunction Solar Cells. *ACS Appl. Mater. Interfaces* **2017**, *9*, 3223–3245.
- (95) Bellani, S.; Najafi, L.; Capasso, A.; Del Rio Castillo, A. E.; Antognazza, M. R.; Bonaccorso, F. Few-Layer MoS₂ Flakes as a Hole-Selective Layer for Solution-Processed Hybrid Organic Hydrogen-Evolving Photocathodes. *J Mater Chem A* **2017**, *5*, 4384–4396.
- (96) Capasso, A.; Del Rio Castillo, A. E.; Najafi, L.; Pellegrini, V.; Bonaccorso, F.; Matteocci, F.; Cinà, L.; Di Carlo, A. Spray Deposition of Exfoliated MoS₂ Flakes as Hole Transport Layer in Perovskite-Based Photovoltaics. In *2015 IEEE 15th International Conference on Nanotechnology (IEEE-NANO)*; 2015; pp 1138–1141.
- (97) Kohnehpoushi, S.; Nazari, P.; Nejand, B. A.; Eskandari, M. MoS₂: A Two-Dimensional Hole-Transporting Material for High-Efficiency, Low-Cost Perovskite Solar Cells. *Nanotechnology* **2018**, *29*, 205201.
- (98) Xing, G.; Wei, C.; Hai, L.; Zhongwei, W.; Zhiyuan, Z.; Shuit-Tong, L.; Hua, Z.; Baoquan, S. A Solution-Processed Hole Extraction Layer Made from Ultrathin MoS₂ Nanosheets for Efficient Organic Solar Cells. *Adv. Energy Mater.* **2013**, *3*, 1262–1268.
- (99) Xing, W.; Chen, Y.; Wang, X.; Lv, L.; Ouyang, X.; Ge, Z.; Huang, H. MoS₂ Quantum Dots with a Tunable Work Function for High-Performance Organic Solar Cells. *ACS Appl. Mater. Interfaces* **2016**, *8*, 26916–26923.
- (100) Wu, Z.; Bai, S.; Xiang, J.; Yuan, Z.; Yang, Y.; Cui, W.; Gao, X.; Liu, Z.; Jin, Y.; Sun, B. Efficient Planar Heterojunction Perovskite Solar Cells Employing Graphene Oxide as Hole Conductor. *Nanoscale* **2014**, *6*, 10505–10510.
- (101) Yan, K.; Wei, Z.; Li, J.; Chen, H.; Yi, Y.; Zheng, X.; Long, X.; Wang, Z.; Wang, J.; Xu, J.; Yang, S. High-Performance Graphene-Based Hole Conductor-Free Perovskite Solar Cells: Schottky Junction Enhanced Hole Extraction and Electron Blocking. *Small* **2015**, *11*, 2269–2274.
- (102) Palma, A. L.; Cinà, L.; Pescetelli, S.; Agresti, A.; Raggio, M.; Paolesse, R.; Bonaccorso, F.; Di Carlo, A. Reduced Graphene Oxide as Efficient and Stable Hole Transporting Material in Mesoscopic Perovskite Solar Cells. *Nano Energy* **2016**, *22*, 349–360.
- (103) Yeo, J.-S.; Kang, R.; Lee, S.; Jeon, Y.-J.; Myoung, N.; Lee, C.-L.; Kim, D.-Y.; Yun, J.-M.; Seo, Y.-H.; Kim, S.-S.; Na, S. I. Highly Efficient and Stable Planar Perovskite Solar Cells with Reduced Graphene Oxide Nanosheets as Electrode Interlayer. *Nano Energy* **2015**, *12*, 96–104.
- (104) Arora, N.; Dar, M. I.; Hinderhofer, A.; Pellet, N.; Schreiber, F.; Zakeeruddin, S. M.; Grätzel, M. Perovskite Solar Cells with CuSCN Hole Extraction Layers Yield Stabilized Efficiencies Greater than 20%. *Science* **2017**, *358*, 768–771.

- (105) Nouri, E.; Wang, Y.-L.; Chen, Q.; Xu, J.-J.; Paterakis, G.; Dracopoulos, V.; Xu, Z.-X.; Tasis, D.; Mohammadi, M. R.; Lianos, P. Introduction of Graphene Oxide as Buffer Layer in Perovskite Solar Cells and the Promotion of Soluble N-Butyl-Substituted Copper Phthalocyanine as Efficient Hole Transporting Material. *Electrochimica Acta* **2017**, *233*, 36–43.
- (106) Lee, S. Y.; Kim, U. J.; Chung, J.; Nam, H.; Jeong, H. Y.; Han, G. H.; Kim, H.; Oh, H. M.; Lee, H.; Kim, H.; Roh, Y. G. Large Work Function Modulation of Monolayer MoS₂ by Ambient Gases. *ACS Nano* **2016**, *10*, 6100–6107.
- (107) Zhou, P.; Song, X.; Yan, X.; Liu, C.; Chen, L.; Sun, Q.; Zhang, D. W. Controlling the Work Function of Molybdenum Disulfide by *in Situ* Metal Deposition. *Nanotechnology* **2016**, *27*, 344002.
- (108) Baik, S. S.; Im, S.; Choi, H. J. Work Function Tuning in Two-Dimensional MoS₂ Field-Effect-Transistors with Graphene and Titanium Source-Drain Contacts. *Sci. Rep.* **2017**, *7*, 45546.
- (109) Kim, J. H.; Lee, J.; Kim, J. H.; Hwang, C. C.; Lee, C.; Park, J. Y. Work Function Variation of MoS₂ Atomic Layers Grown with Chemical Vapor Deposition: The Effects of Thickness and the Adsorption of Water/oxygen Molecules. *Appl. Phys. Lett.* **2015**, *106*, 251606.
- (110) Shi, Y.; Kim, K. K.; Reina, A.; Hofmann, M.; Li, L.-J.; Kong, J. Work Function Engineering of Graphene Electrode *via* Chemical Doping. *ACS Nano* **2010**, *4*, 2689–2694.
- (111) Chang, K. K.; Soon, C. K.; Young, K. S. Increased Work Function in Few-Layer Graphene Sheets *via* Metal Chloride Doping. *Adv. Funct. Mater.* **2012**, *22*, 4724–4731.
- (112) Garg, R.; Dutta, K. N.; Choudhury, R. N. Work Function Engineering of Graphene. *Nanomaterials* **2014**, *4*, 267.
- (113) Sygellou, L.; Paterakis, G.; Galiotis, C.; Tasis, D. Work Function Tuning of Reduced Graphene Oxide Thin Films. *J. Phys. Chem. C* **2016**, *120*, 281–290.
- (114) Harwell, J. R.; Baikie, T. K.; Baikie, I. D.; Payne, J. L.; Ni, C.; Irvine, J. T. S.; Turnbull, G. A.; Samuel, I. D. W. Probing the Energy Levels of Perovskite Solar Cells *via* Kelvin Probe and UV Ambient Pressure Photoemission Spectroscopy. *Phys. Chem. Chem. Phys.* **2016**, *18*, 19738–19745.
- (115) Nguyen, W. H.; Bailie, C. D.; Unger, E. L.; McGehee, M. D. Enhancing the Hole-Conductivity of Spiro-OMeTAD without Oxygen or Lithium Salts by Using Spiro(TFSI)₂ in Perovskite and Dye-Sensitized Solar Cells. *J. Am. Chem. Soc.* **2014**, *136*, 10996–11001.
- (116) Saygili, Y.; Turren-Cruz, S. H.; Olthof, S.; Saes, B. W. H.; Pehlivan, I. B.; Saliba, M.; Meerholz, K.; Edvinsson, T.; Zakeeruddin, S. M.; Grätzel, M.; Correa-Baena, J. P. Planar Perovskite Solar Cells with High Open-Circuit Voltage Containing a Supramolecular Iron Complex as Hole Transport Material Dopant. *ChemPhysChem* **2018**, *19*, 1363–1370.
- (117) Schölin, R.; Karlsson, M. H.; Eriksson, S. K.; Siegbahn, H.; Johansson, E. M. J.; Rensmo, H. Energy Level Shifts in Spiro-OMeTAD Molecular Thin Films When Adding Li-TFSI. *J. Phys. Chem. C* **2012**, *116*, 26300–26305.
- (118) Nardes, A. M.; Kemerink, M.; de Kok, M. M.; Vinken, E.; Maturova, K.; Janssen, R. A. J. Conductivity, Work Function, and Environmental Stability of PEDOT:PSS Thin Films Treated with Sorbitol. *Org. Electron.* **2008**, *9*, 727–734.
- (119) J. Huang, J.; Miller, P.F.; Wilson, J.S.; de Mello, A.J.; de Mello, J.C.; Bradley, D.D.C. Investigation of the Effects of Doping and Post-Deposition Treatments on the Conductivity, Morphology, and Work Function of Poly(3,4-ethylenedioxythiophene)/Poly(styrene Sulfonate) Films. *Adv. Funct. Mater.* **2005**, *15*, 290–296.
- (120) Hwang, J.; Amy, F.; Kahn, A. Spectroscopic Study on Sputtered PEDOT·PSS: Role of Surface PSS Layer. *Org. Electron.* **2006**, *7*, 387–396.
- (121) Brown, T. M.; Kim, J. S.; Friend, R. H.; Cacialli, F.; Daik, R.; Feast, W. J. Built-in Field Electroabsorption Spectroscopy of Polymer Light-Emitting Diodes Incorporating a Doped

- poly(3,4-Ethylene Dioxythiophene) Hole Injection Layer. *Appl. Phys. Lett.* **1999**, *75*, 1679–1681.
- (122) Jun, L.; Yuhua, X.; Yunxiang, G.; Dingshan, Y.; Michael, D.; Liming, D. Hole and Electron Extraction Layers Based on Graphene Oxide Derivatives for High-Performance Bulk Heterojunction Solar Cells. *Adv. Mater.* **2012**, *24*, 2228–2233.
- (123) Lin, Y.; Li, X.; Xie, D.; Feng, T.; Chen, Y.; Song, R.; Tian, H.; Ren, T.; Zhong, M.; Wang, K.; Zhu, H. Graphene/semiconductor Heterojunction Solar Cells with Modulated Antireflection and Graphene Work Function. *Energy Environ. Sci.* **2013**, *6*, 108–115.
- (124) Huang, H.; Li, Z.; She, J.; Wang, W. Oxygen Density Dependent Band Gap of Reduced Graphene Oxide. *J. Appl. Phys.* **2012**, *111*, 54317.
- (125) Shen, Y.; Yang, S.; Zhou, P.; Sun, Q.; Wang, P.; Wan, L.; Li, J.; Chen, L.; Wang, X.; Ding, S.; Zhang, D. W. Evolution of the Band-Gap and Optical Properties of Graphene Oxide with Controllable Reduction Level. *Carbon* **2013**, *62*, 157–164.
- (126) Ellis, J. K.; Lucero, M. J.; Scuseria, G. E. The Indirect to Direct Band Gap Transition in Multilayered MoS₂ as Predicted by Screened Hybrid Density Functional Theory. *Appl. Phys. Lett.* **2011**, *99*, 261908.
- (127) Yun, W. S.; Han, S. W.; Hong, S. C.; Kim, I. G.; Lee, J. D. Thickness and Strain Effects on Electronic Structures of Transition Metal Dichalcogenides: 2H-MX₂ Semiconductors (M = Mo, W; X = S, Se, Te). *Phys. Rev. B* **2012**, *85*, 033305.
- (128) Mak, K. F.; Lee, C.; Hone, J.; Shan, J.; Heinz, T. F. Atomically Thin MoS₂: A New Direct-Gap Semiconductor. *Phys. Rev. Lett.* **2010**, *105*, 136805.
- (129) Han, S. W.; Kwon, H.; Kim, S. K.; Ryu, S.; Yun, W. S.; Kim, D. H.; Hwang, J. H.; Kang, J.-S.; Baik, J.; Shin, H. J.; Hong, S. C. Band-Gap Transition Induced by Interlayer van Der Waals Interaction in MoS₂. *Phys. Rev. B* **2011**, *84*, 045409.
- (130) Wang, Q. H.; Kalantar-Zadeh, K.; Kis, A.; Coleman, J. N.; Strano, M. S. Electronics and Optoelectronics of Two-Dimensional Transition Metal Dichalcogenides. *Nat. Nanotechnol.* **2012**, *7*, 699.
- (131) Kang, J.; Tongay, S.; Zhou, J.; Li, J.; Wu, J. Band Offsets and Heterostructures of Two-Dimensional Semiconductors. *Appl. Phys. Lett.* **2013**, *102*, 12111.
- (132) Wu, M.; Yao, X.; Hao, Y.; Dong, H.; Cheng, Y.; Liu, H.; Lu, F.; Wang, W.; Cho, K.; Wang, W.-H. Electronic Structures, Magnetic Properties and Band Alignments of 3d Transition Metal Atoms Doped Monolayer MoS₂. *Phys. Lett. A* **2018**, *382*, 111–115.
- (133) Rasmussen, F. A.; Thygesen, K. S. Computational 2D Materials Database: Electronic Structure of Transition-Metal Dichalcogenides and Oxides. *J. Phys. Chem. C* **2015**, *119*, 13169–13183.
- (134) Qiu, J.; Qiu, Y.; Yan, K.; Zhong, M.; Mu, C.; Yan, H.; Yang, S. All-Solid-State Hybrid Solar Cells Based on a New Organometal Halide Perovskite Sensitizer and One-Dimensional TiO₂ Nanowire Arrays. *Nanoscale* **2013**, *5*, 3245–3248.
- (135) Yang, G.; Tao, H.; Qin, P.; Ke, W.; Fang, G. Recent Progress in Electron Transport Layers for Efficient Perovskite Solar Cells. *J. Mater. Chem. A* **2016**, *4*, 3970–3990.
- (136) Kim, H.-S.; Lee, C.-R.; Im, J.-H.; Lee, K.-B.; Moehl, T.; Marchioro, A.; Moon, S.-J.; Humphry-Baker, R.; Yum, J.-H.; Moser, J. E.; Grätzel, M. Lead Iodide Perovskite Sensitized All-Solid-State Submicron Thin Film Mesoscopic Solar Cell with Efficiency Exceeding 9%. *Sci. Rep.* **2012**, *2*, 591.
- (137) Hao, F.; Stoumpos, C. C.; Chang, R. P. H.; Kanatzidis, M. G. Anomalous Band Gap Behavior in Mixed Sn and Pb Perovskites Enables Broadening of Absorption Spectrum in Solar Cells. *J. Am. Chem. Soc.* **2014**, *136*, 8094–8099.
- (138) Olthof, S. Research Update: The Electronic Structure of Hybrid Perovskite Layers and Their Energetic Alignment in Devices. *APL Mater.* **2016**, *4*, 91502.

- (139) Philip, S.; L., W.-B. L.; A., M. B.; C., O. D.; Yueh-Lin, L.; Antoine, K. Electronic Level Alignment in Inverted Organometal Perovskite Solar Cells. *Adv. Mater. Interfaces* **2015**, *2*, 1400532.
- (140) Ratcliff, E. L.; Garcia, A.; Paniagua, S. A.; Cowan, S. R.; Giordano, A. J.; Ginley, D. S.; Marder, S. R.; Berry, J. J.; Olson, D. C. Investigating the Influence of Interfacial Contact Properties on Open Circuit Voltages in Organic Photovoltaic Performance: Work Function Versus Selectivity. *Adv. Energy Mater.* **2013**, *3*, 647–656.
- (141) Steim, R.; Choulis, S. A.; Schilinsky, P.; Brabec, C. J. Interface Modification for Highly Efficient Organic Photovoltaics. *Appl. Phys. Lett.* **2008**, *92*, 93303.
- (142) Zhong, H.; Quhe, R.; Wang, Y.; Ni, Z.; Ye, M.; Song, Z.; Pan, Y.; Yang, J.; Yang, L.; Lei, M.; Shi, J. Interfacial Properties of Monolayer and Bilayer MoS₂ Contacts with Metals: Beyond the Energy Band Calculations. *Sci. Rep.* **2016**, *6*, 21786.
- (143) Yun, J.-M.; Noh, Y.-J.; Yeo, J.-S.; Go, Y.-J.; Na, S.-I.; Jeong, H.-G.; Kim, J.; Lee, S.; Kim, S.-S.; Koo, H. Y.; Kim, T. W. Efficient Work-Function Engineering of Solution-Processed MoS₂ Thin-Films for Novel Hole and Electron Transport Layers Leading to High-Performance Polymer Solar Cells. *J Mater Chem C* **2013**, *1*, 3777–3783.
- (144) Najafi, L.; Bellani, S.; Martín-García, B.; Oropesa-Nuñez, R.; Del Rio Castillo, A. E.; Prato, M.; Moreels, I.; Bonaccorso, F. Solution-Processed Hybrid Graphene Flake/2H-MoS₂ Quantum Dot Heterostructures for Efficient Electrochemical Hydrogen Evolution. *Chem. Mater.* **2017**, *29*, 5782–5786.
- (145) Sun, Y.; Takacs, C. J.; Cowan, S. R.; Seo, J. H.; Gong, X.; Roy, A.; Heeger, A. J. Efficient, Air-Stable Bulk Heterojunction Polymer Solar Cells Using MoO_x as the Anode Interfacial Layer. *Adv. Mater.* **2011**, *23*, 2226–2230.
- (146) Fumagalli, F.; Bellani, S.; Schreier, M.; Leonardi, S.; Rojas, H. C.; Ghadirzadeh, A.; Tullii, G.; Savoini, A.; Marra, G.; Meda, L.; Grätzel, M.; Lanzani, G.; Mayer, M. T., Antognazza, M. R.; Di Fonzo, F. Hybrid Organic–inorganic H₂-Evolving Photocathodes: Understanding the Route towards High Performance Organic Photoelectrochemical Water Splitting. *J Mater Chem A* **2016**, *4*, 2178–2187.
- (147) Chen, L.-M.; Xu, Z.; Hong, Z.; Yang, Y. Interface Investigation and Engineering – Achieving High Performance Polymer Photovoltaic Devices. *J. Mater. Chem.* **2010**, *20*, 2575.
- (148) Lu, C.-P.; Li, G.; Mao, J.; Wang, L.-M.; Andrei, E. Y. Bandgap, Mid-Gap States, and Gating Effects in MoS₂. *Nano Lett.* **2014**, *14*, 4628–4633.
- (149) Fivaz, R.; Mooser, E. Mobility of Charge Carriers in Semiconducting Layer Structures. *Phys. Rev.* **1967**, *163*, 743–755.
- (150) H., E.-M. S.; L., E. B. Temperature Dependence of the Electrical Conductivity and Hall Coefficient in 2H-MoS₂, MoSe₂, WSe₂, and MoTe₂. *Phys. Status Solidi B* **2018**, *79*, 713–722.
- (151) Dolui, K.; Rungger, I.; Sanvito, S. Origin of the N-Type and P-Type Conductivity of MoS₂ Monolayers on a SiO₂ Substrate. *Phys. Rev. B* **2013**, *87*, 165402.
- (152) Yuan, S.; Roldán, R.; Katsnelson, M. I.; Guinea, F. Effect of Point Defects on the Optical and Transport Properties of MoS₂ and WS₂. *Phys. Rev. B* **2014**, *90*, 041402.
- (153) Vancsó, P.; Magda, G. Z.; Pető, J.; Noh, J.-Y.; Kim, Y.-S.; Hwang, C.; Biró, L. P.; Tapasztó, L. The Intrinsic Defect Structure of Exfoliated MoS₂ Single Layers Revealed by Scanning Tunneling Microscopy. *Sci. Rep.* **2016**, *6*, 29726.
- (154) Cho, K.; Min, M.; Kim, T.-Y.; Jeong, H.; Pak, J.; Kim, J.-K.; Jang, J.; Yun, S. J.; Lee, Y. H.; Hong, W.-K.; Lee, T. Electrical and Optical Characterization of MoS₂ with Sulfur Vacancy Passivation by Treatment with Alkanethiol Molecules. *ACS Nano* **2015**, *9*, 8044–8053.
- (155) Liu, D.; Guo, Y.; Fang, L.; Robertson, J. Sulfur Vacancies in Monolayer MoS₂ and Its Electrical Contacts. *Appl. Phys. Lett.* **2013**, *103*, 183113.
- (156) Le, D.; Rawal, T. B.; Rahman, T. S. Single-Layer MoS₂ with Sulfur Vacancies: Structure and Catalytic Application. *J. Phys. Chem. C* **2014**, *118*, 5346–5351.

- (157) Qiu, H.; Xu, T.; Wang, Z.; Ren, W.; Nan, H.; Ni, Z.; Chen, Q.; Yuan, S.; Miao, F.; Song, F.; Long, G. Hopping Transport through Defect-Induced Localized States in Molybdenum Disulphide. *Nat. Commun.* **2013**, *4*, 2642.
- (158) Fabbri, F.; Rotunno, E.; Cinquanta, E.; Campi, D.; Bonnini, E.; Kaplan, D.; Lazzarini, L.; Bernasconi, M.; Ferrari, C.; Longo, M.; Nicotra, G. Novel near-Infrared Emission from Crystal Defects in MoS₂ Multilayer Flakes. *Nat. Commun.* **2016**, *7*, 13044.
- (159) Yin, Z.; Li, H.; Li, H.; Jiang, L.; Shi, Y.; Sun, Y.; Lu, G.; Zhang, Q.; Chen, X.; Zhang, H. Single-Layer MoS₂ Phototransistors. *ACS Nano* **2012**, *6*, 74–80.
- (160) Yung-Chang, L.; O., D. D.; Hannu-Pekka, K.; Yoshiko, N.; V., K. A.; Ying-Sheng, H.; Kazu, S. Properties of Individual Dopant Atoms in Single-Layer MoS₂: Atomic Structure, Migration, and Enhanced Reactivity. *Adv. Mater.* **2014**, *26*, 2857–2861.
- (161) Baugher, B. W. H.; Churchill, H. O. H.; Yang, Y.; Jarillo-Herrero, P. Intrinsic Electronic Transport Properties of High-Quality Monolayer and Bilayer MoS₂. *Nano Lett.* **2013**, *13*, 4212–4216.
- (162) McDonnell, S.; Addou, R.; Buie, C.; Wallace, R. M.; Hinkle, C. L. Defect-Dominated Doping and Contact Resistance in MoS₂. *ACS Nano* **2014**, *8*, 2880–2888.
- (163) Zhou, W.; Zou, X.; Najmaei, S.; Liu, Z.; Shi, Y.; Kong, J.; Lou, J.; Ajayan, P. M.; Yakobson, B. I.; Idrobo, J.-C. Intrinsic Structural Defects in Monolayer Molybdenum Disulfide. *Nano Lett.* **2013**, *13*, 2615–2622.
- (164) Santosh KC; Roberto C Longo; Rafik Addou; Robert M Wallace; Kyeongjae Cho. Impact of Intrinsic Atomic Defects on the Electronic Structure of MoS₂ Monolayers. *Nanotechnology* **2014**, *25*, 375703.
- (165) Zhao, Y.; Nardes, A. M.; Zhu, K. Solid-State Mesostuctured Perovskite CH₃NH₃PbI₃ Solar Cells: Charge Transport, Recombination, and Diffusion Length. *J. Phys. Chem. Lett.* **2014**, *5*, 490–494.
- (166) Martín-García, B.; Polovitsyn, A.; Prato, M.; Moreels, I. Efficient Charge Transfer in Solution-Processed PbS Quantum Dot–reduced Graphene Oxide Hybrid Materials. *J. Mater. Chem. C* **2015**, *3*, 7088–7095.
- (167) Hou, S.; Su, S.; Kasner, M. L.; Shah, P.; Patel, K.; Madarang, C. J. Formation of Highly Stable Dispersions of Silane-Functionalized Reduced Graphene Oxide. *Chem. Phys. Lett.* **2010**, *501*, 68–74.
- (168) Yao, H.; Jin, L.; Sue, H.-J.; Sumi, Y.; Nishimura, R. Facile Decoration of Au Nanoparticles on Reduced Graphene Oxide Surfaces *via* a One-Step Chemical Functionalization Approach. *J. Mater. Chem. A* **2013**, *1*, 10783.
- (169) Chen, X.; Berner, N. C.; Backes, C.; Duesberg, G. S.; McDonald, A. R. Functionalization of Two-Dimensional MoS₂: On the Reaction Between MoS₂ and Organic Thiols. *Angew. Chem. Int. Ed.* **2016**, *55*, 5803–5808.
- (170) Förster, A.; Gemming, S.; Seifert, G.; Tománek, D. Chemical and Electronic Repair Mechanism of Defects in MoS₂ Monolayers. *ACS Nano* **2017**, *11*, 9989–9996.
- (171) Ding, Q.; Czech, K. J.; Zhao, Y.; Zhai, J.; Hamers, R. J.; Wright, J. C.; Jin, S. Basal-Plane Ligand Functionalization on Semiconducting 2H-MoS₂ Monolayers. *ACS Appl. Mater. Interfaces* **2017**, *9*, 12734–12742.
- (172) Green, A. A.; Hersam, M. C. Solution Phase Production of Graphene with Controlled Thickness *via* Density Differentiation. *Nano Lett.* **2009**, *9*, 4031–4036.
- (173) Sun, X.; Luo, D.; Liu, J.; Evans, D. G. Monodisperse Chemically Modified Graphene Obtained by Density Gradient Ultracentrifugal Rate Separation. *ACS Nano* **2010**, *4*, 3381–3389.
- (174) Björkman, T.; Gulans, A.; Krasheninnikov, A. V.; Nieminen, R. M. Van Der Waals Bonding in Layered Compounds from Advanced Density-Functional First-Principles Calculations. *Phys. Rev. Lett.* **2012**, *108*, 235502.

- (175) Toulhoat, P. R. and G. K. and J. H. and H. *Ab Initio* Density Functional Studies of Transition-Metal Sulphides: I. Crystal Structure and Cohesive Properties. *J. Phys. Condens. Matter* **1997**, *9*, 11085.
- (176) Bučko, T.; Hafner, J.; Lebègue, S.; Ángyán, J. G. Improved Description of the Structure of Molecular and Layered Crystals: *Ab Initio* DFT Calculations with van Der Waals Corrections. *J. Phys. Chem. A* **2010**, *114*, 11814–11824.
- (177) Jawaid, A.; Nepal, D.; Park, K.; Jespersen, M.; Qualley, A.; Mirau, P.; Drummy, L. F.; Vaia, R. A. Mechanism for Liquid Phase Exfoliation of MoS₂. *Chem. Mater.* **2016**, *28*, 337–348.
- (178) Shen, J.; He, Y.; Wu, J.; Gao, C.; Keyshar, K.; Zhang, X.; Yang, Y.; Ye, M.; Vajtai, R.; Lou, J.; Ajayan, P. M.. Liquid Phase Exfoliation of Two-Dimensional Materials by Directly Probing and Matching Surface Tension Components. *Nano Lett.* **2015**, *15*, 5449–5454.
- (179) Bonaccorso, F.; Zerbetto, M.; Ferrari, A. C.; Amendola, V. Sorting Nanoparticles by Centrifugal Fields in Clean Media. *J. Phys. Chem. C* **2013**, *117*, 13217–13229.
- (180) Gao, X.; Jang, J.; Nagase, S. Hydrazine and Thermal Reduction of Graphene Oxide: Reaction Mechanisms, Product Structures, and Reaction Design. *J. Phys. Chem. C* **2010**, *114*, 832–842.
- (181) Pei, S.; Cheng, H.-M. The Reduction of Graphene Oxide. *Carbon* **2012**, *50*, 3210–3228.
- (182) Hummers, W. S.; Offeman, R. E. Preparation of Graphitic Oxide. *J. Am. Chem. Soc.* **1958**, *80*, 1339.
- (183) Bellani, S.; Najafi, L.; Martín-García, B.; Ansaldo, A.; Del Rio Castillo, A. E.; Prato, M.; Moreels, I.; Bonaccorso, F. Graphene-Based Hole-Selective Layers for High-Efficiency, Solution-Processed, Large-Area, Flexible, Hydrogen-Evolving Organic Photocathodes. *J. Phys. Chem. C* **2017**, *121*, 21887–21903.
- (184) Zhang, X.; Coleman, A. C.; Katsonis, N.; Browne, W. R.; van Wees, B. J.; Feringa, B. L. Dispersion of Graphene in Ethanol Using a Simple Solvent Exchange Method. *Chem Commun* **2010**, *46*, 7539–7541.
- (185) Sun, H.; Del Rio Castillo, A. E.; Monaco, S.; Capasso, A.; Ansaldo, A.; Prato, M.; Dinh, D. A.; Pellegrini, V.; Scrosati, B.; Manna, L.; Bonaccorso, F. Binder-Free Graphene as an Advanced Anode for Lithium Batteries. *J Mater Chem A* **2016**, *4*, 6886–6895.
- (186) Gao, W. The Chemistry of Graphene Oxide: Graphene Oxide: Reduction Recipes, Spectroscopy, and Applications; Gao, W., Ed.; Springer International Publishing: Cham, 2015; pp 61–95.
- (187) Pham, N. P.; Burghartz, J. N.; Sarro, P. M. Spray Coating of Photoresist for Pattern Transfer on High Topography Surfaces. *J. Micromechanics Microengineering* **2005**, *15*, 691.
- (188) Song, Z.; McElvany, C. L.; Phillips, A. B.; Celik, I.; Krantz, P. W.; Wathage, S. C.; Liyanage, G. K.; Apul, D.; Heben, M. J. A Technoeconomic Analysis of Perovskite Solar Module Manufacturing with Low-Cost Materials and Techniques. *Energy Environ. Sci* **2017**, *10*, 1297–1305.
- (189) Yang, Z.; Zhang, S.; Li, L.; Chen, W. Research Progress on Large-Area Perovskite Thin Films and Solar Modules. *J. Materiomics* **2017**, *3*, 231–244.
- (190) Ono, L. K.; Park, N.-G.; Zhu, K.; Huang, W.; Qi, Y. Perovskite Solar Cells—Towards Commercialization. *ACS Energy Lett.* **2017**, *2*, 1749–1751.
- (191) Berry, J. J.; van de Lagemaat, J.; Al-Jassim, M. M.; Kurtz, S.; Yan, Y.; Zhu, K. Perovskite Photovoltaics: The Path to a Printable Terawatt-Scale Technology. *ACS Energy Lett.* **2017**, *2*, 2540–2544.
- (192) Lee, C.; Yan, H.; Brus, L. E.; Heinz, T. F.; Hone, J.; Ryu, S. Anomalous Lattice Vibrations of Single- and Few-Layer MoS₂. *ACS Nano* **2010**, *4*, 2695–2700.
- (193) Huang, Y.; Wu, J.; Hwang, K. C. Thickness of Graphene and Single-Wall Carbon Nanotubes. *Phys. Rev. B* **2006**, *74*, 245413.

- (194) Novoselov, K. S.; Geim, A. K.; Morozov, S. V.; Jiang, D.; Zhang, Y.; Dubonos, S. V.; Grigorieva, I. V.; Firsov, A. A. Electric Field Effect in Atomically Thin Carbon Films. *Science* **2004**, *306*, 666–669.
- (195) Baker, M. A.; Gilmore, R.; Lenardi, C.; Gissler, W. XPS Investigation of Preferential Sputtering of S from MoS₂ and Determination of MoS_x Stoichiometry from Mo and S Peak Positions. *Appl. Surf. Sci.* **1999**, *150*, 255–262.
- (196) Lee, Y. H.; Zhang, X. Q.; Zhang, W.; Chang, M. T.; Lin, C. T.; Chang, K. D.; Yu, Y. C.; Wang, J. T. W.; Chang, C. S.; Li, L. J.; Lin, T. W. Synthesis of Large-Area MoS₂ Atomic Layers with Chemical Vapor Deposition. *Adv. Mater.* **2012**, *24*, 2320–2325.
- (197) Weber, T.; Muijsers, J. C.; van Wolput, J. H. M. C.; Verhagen, C. P. J.; Niemantsverdriet, J. W. Basic Reaction Steps in the Sulfidation of Crystalline MoO₃ to MoS₂, As Studied by X-Ray Photoelectron and Infrared Emission Spectroscopy. *J. Phys. Chem.* **1996**, *100*, 14144–14150.
- (198) Najafi, L.; Bellani, S.; Oropesa-Nuñez, R.; Ansaldo, A.; Prato, M.; Castillo, A. E.D.R.; Bonaccorso, F. Engineered MoSe₂-Based Heterostructures for Efficient Electrochemical Hydrogen Evolution Reaction. *Adv. Energy Mater.* **2018**, *8*, 1703212.
- (199) Bonaccorso, F.; Colombo, L.; Yu, G.; Stoller, M.; Tozzini, V.; Ferrari, A. C.; Ruoff, R. S.; Pellegrini, V. Graphene, Related Two-Dimensional Crystals, and Hybrid Systems for Energy Conversion and Storage. *Science* **2015**, *347*, 1246501.
- (200) Yang, D.; Velamakanni, A.; Bozoklu, G.; Park, S.; Stoller, M.; Piner, R. D.; Stankovich, S.; Jung, I.; Field, D. A.; Ventrice, C. A.; Ruoff, R. S. Chemical Analysis of Graphene Oxide Films after Heat and Chemical Treatments by X-Ray Photoelectron and Micro-Raman Spectroscopy. *Carbon* **2009**, *47*, 145–152.
- (201) Dong, X.; Su, C.-Y.; Zhang, W.; Zhao, J.; Ling, Q.; Huang, W.; Chen, P.; Li, L.-J. Ultra-Large Single-Layer Graphene Obtained from Solution Chemical Reduction and Its Electrical Properties. *Phys Chem Chem Phys* **2010**, *12*, 2164–2169.
- (202) Becerril, H. A.; Stoltenberg, R. M.; Tang, M. L.; Roberts, M. E.; Liu, Z.; Chen, Y.; Kim, D. H.; Lee, B.-L.; Lee, S.; Bao, Z. Fabrication and Evaluation of Solution-Processed Reduced Graphene Oxide Electrodes for P- and N-Channel Bottom-Contact Organic Thin-Film Transistors. *ACS Nano* **2010**, *4*, 6343–6352.
- (203) Ganguly, A.; Sharma, S.; Papakonstantinou, P.; Hamilton, J. Probing the Thermal Deoxygenation of Graphene Oxide Using High-Resolution *In Situ* X-Ray-Based Spectroscopies. *J. Phys. Chem. C* **2011**, *115*, 17009–17019.
- (204) Gao, W.; Alemany, L. B.; Ci, L.; Ajayan, P. M. New Insights into the Structure and Reduction of Graphite Oxide. *Nat. Chem.* **2009**, *1*, 403.
- (205) Johnson, P. A.; Levicky, R. X-Ray Photoelectron Spectroscopy and Differential Capacitance Study of Thiol-Functional Polysiloxane Films on Gold Supports. *Langmuir* **2004**, *20*, 9621–9627.
- (206) Rodriguez, J. A.; Jirsak, T.; Freitag, A.; Hanson, J. C.; Larese, J. Z.; Chaturvedi, S. Interaction of SO₂ with CeO₂ and Cu/CeO₂ Catalysts: Photoemission, XANES and TPD Studies. *Catal. Lett.* **1999**, *62*, 113–119.
- (207) Lee, C. Y.; Le, Q. Van; Kim, C.; Kim, S. Y. Use of Silane-Functionalized Graphene Oxide in Organic Photovoltaic Cells and Organic Light-Emitting Diodes. *Phys Chem Chem Phys* **2015**, *17*, 9369–9374.
- (208) Konios, D.; Stylianakis, M. M.; Stratakis, E.; Kymakis, E. Dispersion Behaviour of Graphene Oxide and Reduced Graphene Oxide. *J. Colloid Interface Sci.* **2014**, *430*, 108–112.
- (209) Wang, S.; Zhang, Y.; Abidi, N.; Cabrales, L. Wettability and Surface Free Energy of Graphene Films. *Langmuir* **2009**, *25*, 11078–11081.
- (210) Jiménez Sandoval, S.; Yang, D.; Frindt, R. F.; Irwin, J. C. Raman Study and Lattice Dynamics of Single Molecular Layers of MoS₂. *Phys. Rev. B* **1991**, *44*, 3955–3962.

- (211) Kopaczek, J.; Polak, M. P.; Scharoch, P.; Wu, K.; Chen, B.; Tongay, S.; Kudrawiec, R. Direct Optical Transitions at K- and H-Point of Brillouin Zone in Bulk MoS₂, MoSe₂, WS₂, and WSe₂. *J. Appl. Phys.* **2016**, *119*, 235705.
- (212) Cheiwchanchamnangij, T.; Lambrecht, W. R. L. Quasiparticle Band Structure Calculation of Monolayer, Bilayer, and Bulk MoS₂. *Phys. Rev. B* **2012**, *85*, 205302.
- (213) Eda, G.; Yamaguchi, H.; Voiry, D.; Fujita, T.; Chen, M.; Chhowalla, M. Photoluminescence from Chemically Exfoliated MoS₂. *Nano Lett.* **2011**, *11*, 5111–5116.
- (214) Zhang, H.; Lu, S. B.; Zheng, J.; Du, J.; Wen, S. C.; Tang, D. Y.; Loh, K. P. Molybdenum Disulfide (MoS₂) as a Broadband Saturable Absorber for Ultra-Fast Photonics. *Opt. Express* **2014**, *22*, 7249–7260.
- (215) Gan, Z. X.; Liu, L. Z.; Wu, H. Y.; Hao, Y. L.; Shan, Y.; Wu, X. L.; Chu, P. K. Quantum Confinement Effects across Two-Dimensional Planes in MoS₂ Quantum Dots. *Appl. Phys. Lett.* **2015**, *106*, 233113.
- (216) Dong, H. H.; Ju, H. D.; Seob, C. J.; Minsu, P.; Seok, S. T. Dual Role of Blue Luminescent MoS₂ Quantum Dots in Fluorescence Resonance Energy Transfer Phenomenon. *Small* **2014**, *10*, 3858–3862.
- (217) Mukherjee, S.; Maiti, R.; Katiyar, A. K.; Das, S.; Ray, S. K. Novel Colloidal MoS₂ Quantum Dot Heterojunctions on Silicon Platforms for Multifunctional Optoelectronic Devices. *Sci. Rep.* **2016**, *6*, 29016.
- (218) Gan, Z.; Xu, H.; Hao, Y. Mechanism for Excitation-Dependent Photoluminescence from Graphene Quantum Dots and Other Graphene Oxide Derivates: Consensus, Debates and Challenges. *Nanoscale* **2016**, *8*, 7794–7807.
- (219) Gopalakrishnan, D.; Damien, D.; Li, B.; Gullappalli, H.; Pillai, V. K.; Ajayan, P. M.; Shaijumon, M. M. Electrochemical Synthesis of Luminescent MoS₂ Quantum Dots. *Chem Commun* **2015**, *51*, 6293–6296.
- (220) Tauc, J. Optical Properties and Electronic Structure of Amorphous Ge and Si. *Mater. Res. Bull.* **1968**, *3*, 37–46.
- (221) Pankove, J. I.; Kiewit, D. A. Optical Processes in Semiconductors. *J. Electrochem. Soc.* **1972**, *5*, 156C-156C
- (222) Mague, J. T. Gmelin Handbook of Inorganic Chemistry. 8th Edition Rh. *Organometallics* 1984.
- (223) Li, T.; Galli, G. Electronic Properties of MoS₂ Nanoparticles. *J. Phys. Chem. C* **2007**, *111*, 16192–16196.
- (224) Lebègue, S.; Eriksson, O. Electronic Structure of Two-Dimensional Crystals from *Ab Initio* Theory. *Phys. Rev. B* **2009**, *79*, 115409.
- (225) Splendiani, A.; Sun, L.; Zhang, Y.; Li, T.; Kim, J.; Chim, C.-Y.; Galli, G.; Wang, F. Emerging Photoluminescence in Monolayer MoS₂. *Nano Lett.* **2010**, *10*, 1271–1275.
- (226) Feng, Y.; Lin, S.; Huang, S.; Shrestha, S.; Conibeer, G. Can Tauc Plot Extrapolation Be Used for Direct-Band-Gap Semiconductor Nanocrystals? *J. Appl. Phys.* **2015**, *117*, 125701.
- (227) Hao, H.; Cuicui, D.; Hongyan, S.; Xun, F.; Jin, L.; Yanlei, T.; Wenbo, S. Water-Soluble Monolayer Molybdenum Disulfide Quantum Dots with Upconversion Fluorescence. *Part. Part. Syst. Charact.* **2014**, *32*, 72–79.
- (228) Sun, Y.; Takacs, C. J.; Cowan, S. R.; Seo, J. H.; Gong, X.; Roy, A.; Heeger, A. J. Efficient, Air-Stable Bulk Heterojunction Polymer Solar Cells Using MoO_x as the Anode Interfacial Layer. *Adv. Mater.* **2011**, *23*, 2226–2230.
- (229) Kröger, M.; Hamwi, S.; Meyer, J.; Riedl, T.; Kowalsky, W.; Kahn, A. Role of the Deep-Lying Electronic States of MoO₃ in the Enhancement of Hole-Injection in Organic Thin Films. *Appl. Phys. Lett.* **2009**, *95*, 123301.
- (230) Balis, N.; Stratakis, E.; Kymakis, E. Graphene and Transition Metal Dichalcogenide Nanosheets as Charge Transport Layers for Solution Processed Solar Cells. *Mater. Today* **2016**, *19*, 580–594.

- (231) Agresti, A.; Pescetelli, S.; Najafi, L.; Del Rio Castillo, A. E.; Oropesa-Nuñez, R.; Busby, Y.; Bonaccorso, F.; Di Carlo, A. Graphene and Related 2D Materials for High Efficient and Stable Perovskite Solar Cells. In *2017 IEEE 17th International Conference on Nanotechnology (IEEE-NANO)*; 2017; pp 145–150.
- (232) Lin, Q.; Armin, A.; Nagiri, R. C. R.; Burn, P. L.; Meredith, P. Electro-Optics of Perovskite Solar Cells. *Nat. Photonics* **2014**, *9*, 106.
- (233) Greiner, M. T.; Lu, Z.-H. Thin-Film Metal Oxides in Organic Semiconductor Devices: Their Electronic Structures, Work Functions and Interfaces. *Npg Asia Mater.* **2013**, *5*, e55.
- (234) Tress, W.; Marinova, N.; Moehl, T.; Zakeeruddin, S. M.; Nazeeruddin, M. K.; Grätzel, M. Understanding the Rate-Dependent J-V Hysteresis, Slow Time Component, and Aging in CH₃NH₃PbI₃ Perovskite Solar Cells: The Role of a Compensated Electric Field. *Energy Environ. Sci.* **2015**, *8*, 995–1004.
- (235) Zhao, Y.; Liang, C.; Zhang, H.; Li, D.; Tian, D.; Li, G.; Jing, X.; Zhang, W.; Xiao, W.; Liu, Q.; Zhang, F. Anomalously Large Interface Charge in Polarity-Switchable Photovoltaic Devices: An Indication of Mobile Ions in Organic-Inorganic Halide Perovskites. *Energy Environ. Sci.* **2015**, *8*, 1256–1260.
- (236) Elumalai, N. K.; Uddin, A. Hysteresis in Organic-Inorganic Hybrid Perovskite Solar Cells. *Sol. Energy Mater. Sol. Cells* **2016**, *157*, 476–509.
- (237) Chen, B.; Yang, M.; Priya, S.; Zhu, K. Origin of J–V Hysteresis in Perovskite Solar Cells. *J. Phys. Chem. Lett.* **2016**, *7*, 905–917.
- (238) Jiménez-López, J.; Cambarau, W.; Cabau, L.; Palomares, E. Charge Injection, Carriers Recombination and HOMO Energy Level Relationship in Perovskite Solar Cells. *Sci. Rep.* **2017**, *7*, 6101.
- (239) Docampo, P.; Ball, J. M.; Darwich, M.; Eperon, G. E.; Snaith, H. J. Efficient Organometal Trihalide Perovskite Planar-Heterojunction Solar Cells on Flexible Polymer Substrates. *Nat. Commun.* **2013**, *4*, 2761.
- (240) Bhosale, J. S.; Moore, J. E.; Wang, X.; Bermel, P.; Lundstrom, M. S. Steady-State Photoluminescent Excitation Characterization of Semiconductor Carrier Recombination. *Rev. Sci. Instrum.* **2016**, *87*, 13104.
- (241) Chang, L.; Kai, W.; Pengcheng, D.; Chao, Y.; Tianyu, M.; Xiong, G. Efficient Solution-Processed Bulk Heterojunction Perovskite Hybrid Solar Cells. *Adv. Energy Mater.* **2015**, *5*, 1402024.
- (242) Wang, X.; Bhosale, J.; Moore, J.; Kapadia, R.; Bermel, P.; Javey, A.; Lundstrom, M. Photovoltaic Material Characterization With Steady State and Transient Photoluminescence. *IEEE J. Photovolt.* **2015**, *5*, 282–287.
- (243) Ginger, D. S.; Greenham, N. C. Photoinduced Electron Transfer from Conjugated Polymers to CdSe Nanocrystals. *Phys. Rev. B* **1999**, *59*, 10622–10629.
- (244) Domanski, K.; Correa-Baena, J.-P.; Mine, N.; Nazeeruddin, M. K.; Abate, A.; Saliba, M.; Tress, W.; Hagfeldt, A.; Grätzel, M. Not All That Glitters Is Gold: Metal-Migration-Induced Degradation in Perovskite Solar Cells. *ACS Nano* **2016**, *10*, 6306–6314.
- (245) Park, N.-G.; Grätzel, M.; Miyasaka, T.; Zhu, K.; Emery, K. Towards Stable and Commercially Available Perovskite Solar Cells. *Nat. Energy* **2016**, *1*, 16152.
- (246) Wang, D.; Wright, M.; Elumalai, N. K.; Uddin, A. Stability of Perovskite Solar Cells. *Sol. Energy Mater. Sol. Cells* **2016**, *147*, 255–275.
- (247) Qin, X.; Zhao, Z.; Wang, Y.; Wu, J.; Jiang, Q.; You, J. Recent Progress in Stability of Perovskite Solar Cells. *J. Semicond.* **2017**, *38*, 11002.
- (248) Berhe, T. A.; Su, W.-N.; Chen, C.-H.; Pan, C.-J.; Cheng, J.-H.; Chen, H.-M.; Tsai, M.-C.; Chen, L.-Y.; Dubale, A. A.; Hwang, B.-J. Organometal Halide Perovskite Solar Cells: Degradation and Stability. *Energy Environ. Sci.* **2016**, *9*, 323–356.

- (249) Wang, Q.; Chen, B.; Liu, Y.; Deng, Y.; Bai, Y.; Dong, Q.; Huang, J. Scaling Behavior of Moisture-Induced Grain Degradation in Polycrystalline Hybrid Perovskite Thin Films. *Energy Environ. Sci.* **2017**, *10*, 516–522.
- (250) Han, Y.; Meyer, S.; Dkhissi, Y.; Weber, K.; Pringle, J. M.; Bach, U.; Spiccia, L.; Cheng, Y.-B. Degradation Observations of Encapsulated Planar CH₃NH₃PbI₃ Perovskite Solar Cells at High Temperatures and Humidity. *J. Mater. Chem. A* **2015**, *3*, 8139–8147.
- (251) Bryant, D.; Aristidou, N.; Pont, S.; Sanchez-Molina, I.; Chotchunangatchaval, T.; Wheeler, S.; Durrant, J. R.; Haque, S. A. Light and Oxygen Induced Degradation Limits the Operational Stability of Methylammonium Lead Triiodide Perovskite Solar Cells. *Energy Environ. Sci.* **2016**, *9*, 1655–1660.
- (252) Aristidou, N.; Sanchez-Molina, I.; Chotchuangchutchaval, T.; Brown, M.; Martinez, L.; Rath, T.; Haque, S. A. The Role of Oxygen in the Degradation of Methylammonium Lead Trihalide Perovskite Photoactive Layers. *Angew. Chem.* **2015**, *127*, 8326–8330.
- (253) Pearson, A. J.; Eperon, G. E.; Hopkinson, P. E.; Habisreutinger, S. N.; Wang, J. T.-W.; Snaith, H. J.; Greenham, N. C. Oxygen Degradation in Mesoporous Al₂O₃/CH₃NH₃PbI_{3-x}Cl_x Perovskite Solar Cells: Kinetics and Mechanisms. *Adv. Energy Mater.* **2016**, *6*, 1600014.
- (254) Nie, W.; Blancon, J.-C.; Neukirch, A. J.; Appavoo, K.; Tsai, H.; Chhowalla, M.; Alam, M. A.; Sfeir, M. Y.; Katan, C.; Even, J.; Tretyak, S. Light-Activated Photocurrent Degradation and Self-Healing in Perovskite Solar Cells. *Nat. Commun.* **2016**, *7*, 11574.
- (255) Docampo, P.; Bein, T. A Long-Term View on Perovskite Optoelectronics. *Acc. Chem. Res.* **2016**, *49*, 339–346.
- (256) Conings, B.; Drijkoningen, J.; Gauquelin, N.; Babayigit, A.; D'Haen, J.; D'Olieslaeger, L.; Ethirajan, A.; Verbeeck, J.; Manca, J.; Mosconi, E.; De Angelis, F. Intrinsic Thermal Instability of Methylammonium Lead Trihalide Perovskite. *Adv. Energy Mater.* **2015**, *5*, 1500477.
- (257) Juarez-Perez, E. J.; Hawash, Z.; Raga, S. R.; Ono, L. K.; Qi, Y. Thermal Degradation of CH₃NH₃PbI₃ Perovskite into NH₃ and CH₃I Gases Observed by Coupled Thermogravimetry-Mass Spectrometry Analysis. *Energy Environ. Sci.* **2016**, *9*, 3406–3410.
- (258) Qiu, L.; Ono, L. K.; Qi, Y. Advances and Challenges to the Commercialization of Organic–inorganic Halide Perovskite Solar Cell Technology. *Mater. Today Energy* **2018**, *7*, 169–189.
- (259) Slavney, A. H.; Smaha, R. W.; Smith, I. C.; Jaffe, A.; Umeyama, D.; Karunadasa, H. I. Chemical Approaches to Addressing the Instability and Toxicity of Lead–Halide Perovskite Absorbers. *Inorg. Chem.* **2017**, *56*, 46–55.
- (260) McMeekin, D. P.; Sadoughi, G.; Rehman, W.; Eperon, G. E.; Saliba, M.; Hörantner, M. T.; Haghighirad, A.; Sakai, N.; Korte, L.; Rech, B.; Johnston, M. B. A Mixed-Cation Lead Mixed-Halide Perovskite Absorber for Tandem Solar Cells. *Science* **2016**, *351*, 151–155.
- (261) Saliba, M.; Matsui, T.; Seo, J.-Y.; Domanski, K.; Correa-Baena, J.-P.; Nazeeruddin, M. K.; Zakeeruddin, S. M.; Tress, W.; Abate, A.; Hagfeldt, A.; Grätzel, M. Cesium-Containing Triple Cation Perovskite Solar Cells: Improved Stability, Reproducibility and High Efficiency. *Energy Environ. Sci.* **2016**, *9*, 1989–1997.
- (262) Saliba, M.; Matsui, T.; Domanski, K.; Seo, J.-Y.; Ummadisingu, A.; Zakeeruddin, S. M.; Correa-Baena, J.-P.; Tress, W. R.; Abate, A.; Hagfeldt, A.; Grätzel, M. Incorporation of Rubidium Cations into Perovskite Solar Cells Improves Photovoltaic Performance. *Science* **2016**, *354*, 206–209.
- (263) Busby, Y.; Agresti, A.; Pescetelli, S.; Di Carlo, A.; Noel, C.; Pireaux, J.-J.; Houssiau, L. Aging Effects in Interface-Engineered Perovskite Solar Cells with 2D Nanomaterials: A Depth Profile Analysis. *Mater. Today Energy* **2018**, *9*, 1–10.
- (264) Jiangwei, L.; Qingshun, D.; Nan, L.; Liduo, W. Direct Evidence of Ion Diffusion for the Silver-Electrode-Induced Thermal Degradation of Inverted Perovskite Solar Cells. *Adv. Energy Mater.* **2017**, *7*, 1602922.

- (265) Cacovich, S.; Cina, L.; Matteocci, F.; Divitini, G.; Midgley, P. A.; Di Carlo, A.; Ducati, C. Gold and Iodine Diffusion in Large Area Perovskite Solar Cells under Illumination. *Nanoscale* **2017**, *9*, 4700–4706.
- (266) Capasso, A.; Matteocci, F.; Najafi, L.; Prato, M.; Buha, J.; Cinà, L.; Pellegrini, V.; Di Carlo, A.; Bonaccorso, F. Few-Layer MoS₂ Flakes as Active Buffer Layer for Stable Perovskite Solar Cells. *Adv. Energy Mater.* **2016**, *6*, 1600920.
- (267) Taheri, B.; Nia, N. Y.; Agresti, A.; Pescetelli, S.; Ciceroni, C.; Castillo, A. E. D. R.; Cinà, L.; Bellani, S.; Bonaccorso, F.; Di Carlo, A. Graphene-Engineered Automated Sprayed Mesoscopic Structure for Perovskite Device Scaling-Up. *2D Mater.* **2018**, DOI: 10.1088/2053-1583/aad983.
- (268) Reese, M. O.; Gevorgyan, S. A.; Jørgensen, M.; Bundgaard, E.; Kurtz, S. R.; Ginley, D. S.; Olson, D. C.; Lloyd, M. T.; Morvillo, P.; Katz, E. A.; Elschner, A. Consensus Stability Testing Protocols for Organic Photovoltaic Materials and Devices. *Sol. Energy Mater. Sol. Cells* **2011**, *95*, 1253–1267.
- (269) Matteocci, F.; Cinà, L.; Lamanna, E.; Cacovich, S.; Divitini, G.; Midgley, P. A.; Ducati, C.; Di Carlo, A. Encapsulation for Long-Term Stability Enhancement of Perovskite Solar Cells. *Nano Energy* **2016**, *30*, 162–172.
- (270) Matteocci, F.; Busby, Y.; Pireaux, J.-J.; Divitini, G.; Cacovich, S.; Ducati, C.; Di Carlo, A. Interface and Composition Analysis on Perovskite Solar Cells. *ACS Appl. Mater. Interfaces* **2015**, *7*, 26176–26183.
- (271) Petridis, C.; Kakavelakis, G.; Kymakis, E. Renaissance of Graphene-Related Materials in Photovoltaics due to the Emergence of Metal Halide Perovskite Solar Cells. *Energy Environ. Sci* **2018**, *11*, 1030–1061.
- (272) Reese, M. O.; Dameron, A. A.; Kempe, M. D. Quantitative Calcium Resistivity Based Method for Accurate and Scalable Water Vapor Transmission Rate Measurement. *Rev. Sci. Instrum.* **2011**, *82*, 85101.

Supporting Information

Morphological analysis of MoS₂ flakes.

Figure S1 reports the morphological analysis (*i.e.*, lateral size and thickness) of the liquid phase exfoliated MoS₂ flakes, from which MoS₂ quantum dots (QDs) were derived by subsequent solvothermal treatment. Figure S1a shows a representative transmission electron microscopy (TEM) image of the MoS₂ flakes, which exhibited regular shaped borders. Figure S1b reports the statistical analysis of lateral dimension of the MoS₂ flakes, which exhibited an average lateral size of ~ 420 nm. Figure S1c shows a representative atomic force microscopy (AFM) image of the MoS₂ flakes. Height profiles (dashed white lines) indicated the presence of one- and two-layer flakes (the monolayer thickness is between 0.7 and 0.8 nm^{1,2}). Figure S1d shows the statistical analysis of the thickness of MoS₂ flakes, which exhibited an average thickness of ~ 2.7 nm.

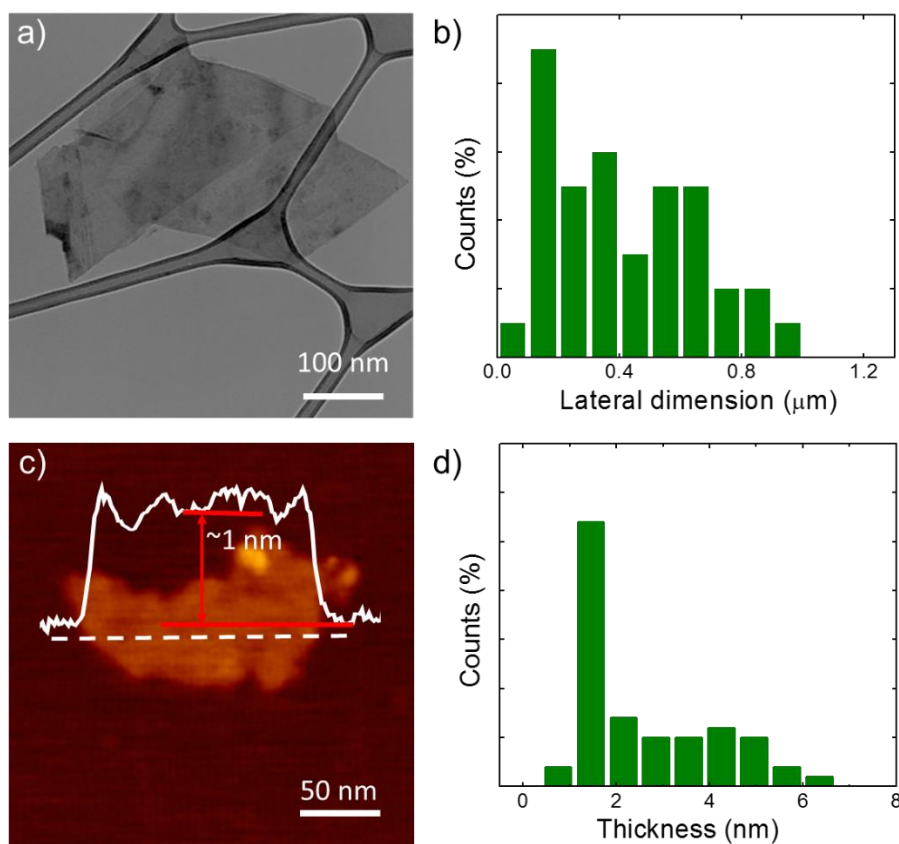


Figure S1. Morphological characterization of the as-produced MoS₂ flakes. (a) TEM image of the MoS₂ flakes. (b) Statistical analysis of the lateral dimension of the MoS₂ flakes (calculated on 100

flakes from different TEM images). (c) AFM image of the MoS₂ flakes. Representative height profile (solid white lines) of the indicated section (white dashed lines) is also shown. (d) Statistical analysis of the thickness of the MoS₂ flakes (calculated on 50 flakes from different AFM images).

Morphological analysis of RGO flakes

Figure S2 reports the morphological analysis of the as-produced reduced graphene oxide (RGO) flakes. Figure S2a shows a representative TEM image of the RGO flakes, which have an irregular shape and rippled structure. Figure S2b reports the statistical analysis of the lateral dimension of the RGO flakes, which have an average value of 1.7 μm . Figure S2c shows a representative AFM image of the RGO flakes. Height profiles (dashed white lines) evidence nano-edge steps between 0.6 and 1.6 nm. Figure S2d shows the statistical analysis of the RGO flakes, which have an average thickness of ~ 1.8 nm. This indicates that few-layer RGO flakes were effectively produced (the monolayer thickness is ~ 0.34 nm^{3,4}).

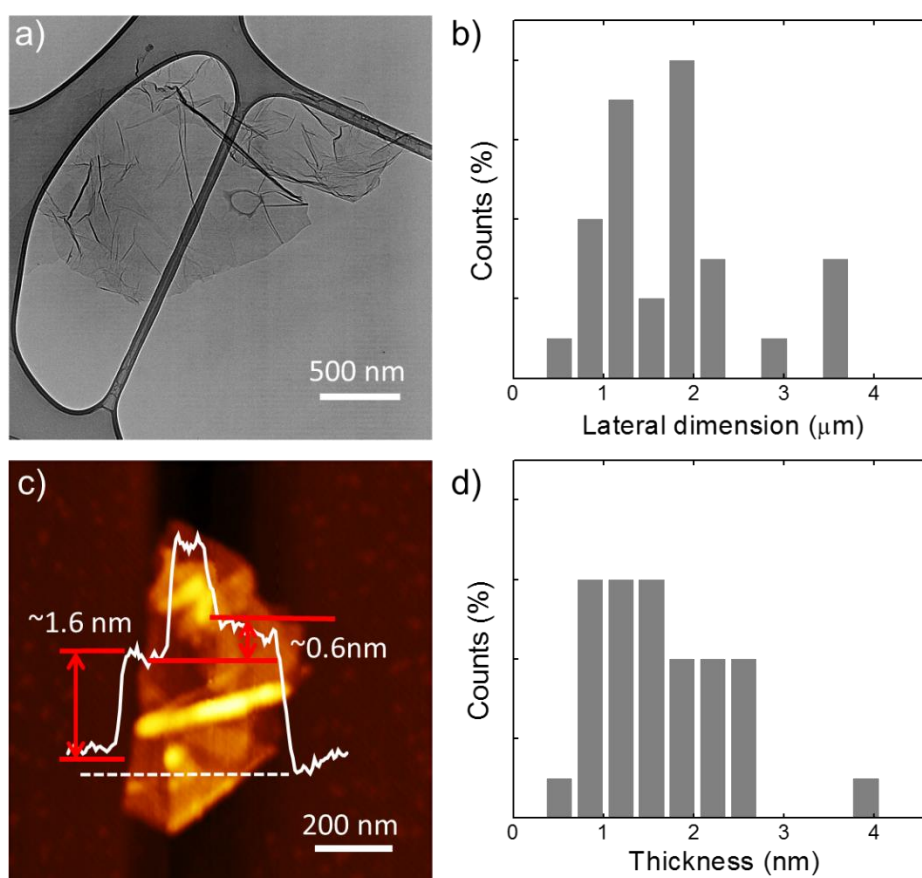


Figure S2. Morphological characterization of the as-produced RGO flakes. (a) TEM image of the RGO flakes. (b) Statistical analysis of the lateral dimension of the RGO flakes (calculated on 100

flakes from different TEM images). (c) AFM image of the RGO flakes. Representative height profile (solid white lines) of the indicated section (white dashed lines) is also shown. (d) Statistical analysis of the thickness of the RGO flakes (calculated on 50 flakes from different AFM images).

Raman spectroscopy characterization of materials

Figure S3a reports representative Raman spectra of MoS₂ QDs, compared to both native bulk MoS₂ powder and MoS₂ flakes. These spectra show the presence of first-order modes at the Brillouin zone center E_{2g}¹(Γ) (~379 cm⁻¹ for both MoS₂ flakes and QDs, and ~377 cm⁻¹ for bulk MoS₂) and A_{1g}(Γ) (~403 cm⁻¹), involving the in-plane displacement of Mo and S atoms and the out-of-plane displacement of S atoms, respectively.^{5,6} The E_{2g}¹(Γ) mode of both the MoS₂ flakes and QDs exhibits softening compared to the one of the bulk MoS₂. The shift of the E_{2g}¹(Γ) mode is explained by the dielectric screening of long-range Coulomb MoS₂ interlayer interaction.⁵ The full width at half maximum (FWHM) of the E_{2g}¹(Γ) and A_{1g}(Γ) (*i.e.*, FWHM(E_{2g}¹(Γ)) and FWHM(A_{1g}(Γ))), respectively) of both MoS₂ flakes and MoS₂ QDs increases of ~3 cm⁻¹ and ~2 cm⁻¹, respectively, compared to the corresponding modes of bulk MoS₂. The increase of FWHM(A_{1g}(Γ)) for MoS₂ flakes and MoS₂ QDs is attributed to the variation of interlayer force constants between the inner and outer layers.²

Figure S3b shows representative Raman spectra of functionalized RGO (f-RGO) flakes, together with its native materials, *i.e.*, graphene oxide (GO) and RGO flakes. The Raman spectrum of GO flakes reveals two main peaks located at 1352 and 1591 cm⁻¹, corresponding to D and G bands, respectively.^{7,8} The G peak corresponds to the E_{2g} phonon at the Brillouin zone center,^{7,8} while the D peak is due to the breathing modes of sp² rings,^{7,8} requiring a defect for its activation by double resonance.⁷ The 2D peak position, located at ~2700 cm⁻¹ is the second order of the D peak.⁹ Double resonance can also happen as an intravalley process, *i.e.*, connecting two points belonging to the same cone around K or K'.⁹ This process gives rise to the D' peak, which is usually located at ~1600 cm⁻¹ in presence of high density defects.⁹ In these conditions, the D' band is merged with the G band. The 2D' peak, located at ~3200 cm⁻¹, is the second order of the D',⁹ while D+D', positioned at ~2940 cm⁻¹

¹ is the combination mode of D and D'. These three peaks show a low intensity, due to electronic scattering,¹⁰ and a very broad line shape. The full width half maximum (FWHM) of D (FWHM(D)) is 127 cm⁻¹, while FWHM(G) is 79 cm⁻¹. The FWHM(G) always increase with disorder and, indeed, it is much larger than pristine graphene (FWHM(G) < 20cm⁻¹)⁸ and edge-defected graphene flakes (FWHM(G) ~ 25cm⁻¹).¹⁰ The high intensity ratio between the intensity of D and G (I_D/I_G) (~0.86) and the large FWHM(D) (~125cm⁻¹) is due to the presence of both structural defects (due to oxidation process) and covalent bonds (e.g., C–H, C–O), both contributing to the D peak. In the case of the RGO flakes, the D and G peaks are located at 1352 cm⁻¹ and 1597 cm⁻¹, respectively, while FWHM(G) and FWHM(D) are 64 cm⁻¹ and 83 cm⁻¹, respectively. The softening of the G band compared to that of GO flakes could be ascribed to the presence of defected regions as consequence of thermal stresses upon annealing.¹¹ FWHM(D) and FWHM(G) are narrower compared to those of GO flakes, indicating a restoration of the sp² rings.⁷ The I_D/I_G for RGO (~1.25) is considerably higher than that of GO flakes (~0.86). In fact, I_G is constant as a function of disorder because is related to the relative motion of sp² carbons,⁷ while an increase of I_D is directly linked to the presence of sp² rings.^{7,8} Thus, an increase of the I_D/I_G means the restoration of sp² rings.⁷ For f-RGO flakes, FWHM(D) and FWHM(G) are further reduced compared to those of the RGO flakes, which means that the sp² rings are preserved.⁷ The I_D/I_G decreases compared to both those of GO and RGO flakes. This effect can be ascribed to the edge/defect passivation of RGO flakes after the functionalization process.^{7,8}

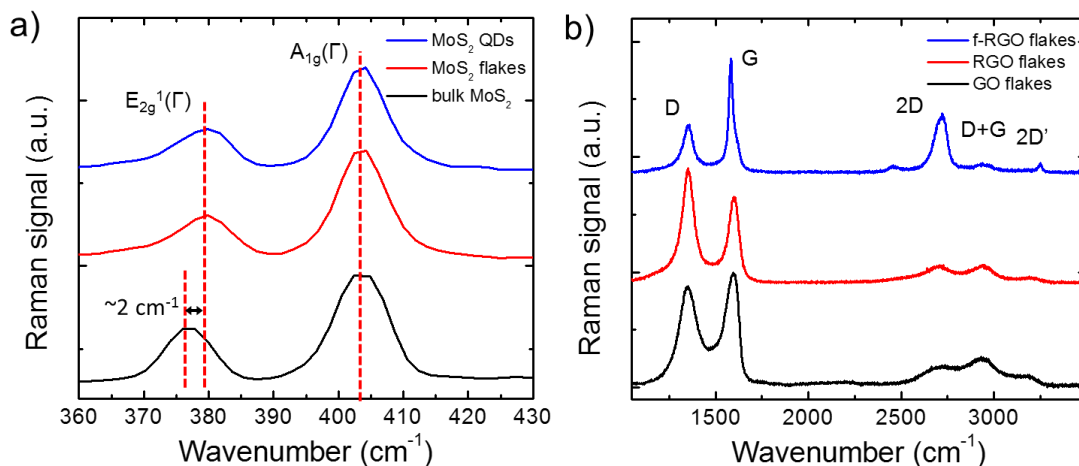


Figure S3. Raman spectra: (a) bulk MoS₂, MoS₂ flakes and MoS₂ QDs; (b) GO flakes, RGO flakes and f-RGO flakes.

Fourier-transform infrared spectroscopy analysis

Fourier-transform infrared (FTIR) spectroscopy was performed on (3-mercaptopropyl)trimethoxysilane (MPTS), RGO, f-RGO, and MoS₂ QDs:f-RGO (**Figure S4**). From the FTIR spectrum of MPTS (**Figure S4a**), it is possible to identify the bands corresponding to Si-O-Si stretching (1089 cm⁻¹), S-H stretching (2564 cm⁻¹) and C-H stretching (2830/2944 cm⁻¹). In agreement with the Scheme 1 of the main text, the first step of the process was the MPTS functionalization of the RGO flakes. As result in the FTIR spectrum of the RGO appeared a broad Si-O-Si stretching band at 1078 cm⁻¹ superimposed to the RGO FTIR spectrum (Figure S4b,c). This observation confirms the hydrolyzation and condensation between the oxygen functionalities of the RGO and the alkoxy silane groups (-OCH₃) during the MPTS functionalization.¹²⁻¹⁴ Notably, the weak peak related to the S-H bond is only shown in the FTIR spectrum of the pure MPTS. This agrees with other studies on the silane functionalization of oxide nanoparticles.¹⁵ In the FTIR spectrum of the MoS₂ QDs:f-RGO, the broad Si-O-Si stretching band of the f-RGO is still at 1078 cm⁻¹. This indicates that the hybridization did not alter the MPTS functionalization of the RGO and, at the same time, that the interaction between MoS₂ QDs and f-RGO only took place at the free SH groups of the MPTS.

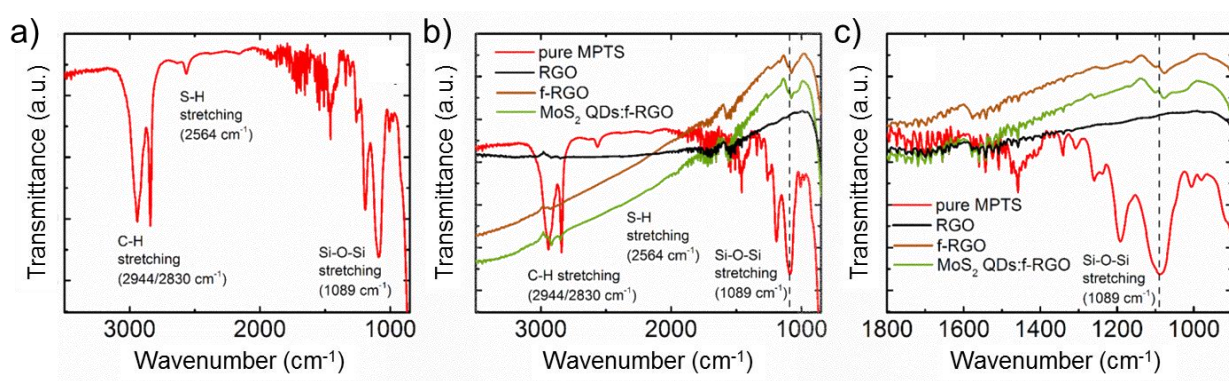


Figure S4. (a) FTIR spectrum of the pure MPTS indicating the main characteristic features: Si-O-Si, S-H and C-H stretching vibrations. (b) Comparison of the FTIR spectra corresponding to pure MPTS, RGO, f-RGO and MoS₂ QDs:f-RGO materials. (c) Corresponding zoom in the Si-O-Si area for the spectra shown in (b).

Gravitational sedimentation of the RGO and f-RGO dispersion in ethanol

Figure S5 shows photographs of 1 mg mL^{-1} RGO and f-RGO dispersions in ethanol (EtOH) after 2 h of gravitational sedimentation. The photographs show a clear sedimentation of the dispersion of RGO due to the poor hydrogen-bonding capability of the as-produced material. After the functionalization of the RGO, the presence of MPTS groups decreased the surface energy of the flakes, making f-RGO compatible with polar solvent, such as EtOH. Consequently, no significant gravitational sedimentation for f-RGO dispersions in EtOH was observed in the same timeframe.

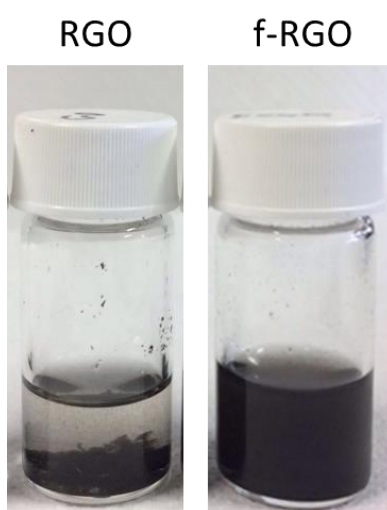


Figure S5. Photograph of 1 mg mL^{-1} RGO and f-RGO dispersions in EtOH after 2 h of gravitational sedimentation.

Photoluminescence analysis of MoS₂ QDs

Figure S6 reports the photoluminescence (PL) spectra of MoS₂ QDs dispersion in 2-Propanol (IPA), collected at different excitation wavelengths (from 300 to 500 nm). The PL peaks were red-shifted with the increase of the excitation wavelength. This excitation-dependent PL emission can be ascribed to quantum confinement and edge state emission effect.¹⁸⁻²⁰ The sharp small features observed in the spectra were related to the IPA solvent, as proved by blank PL spectrum (inset to Figure S6).

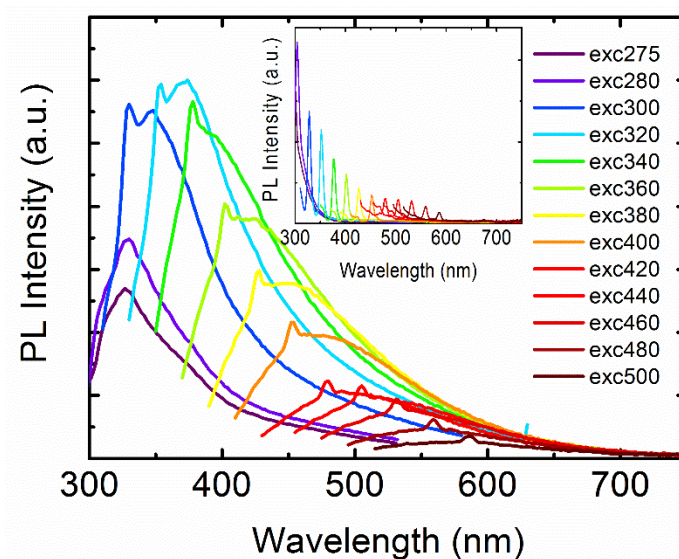


Figure S6. Photoluminescence spectra of the MoS₂ QDs at different excitation wavelength, ranging from 300 to 500 nm. The inset shows the blank (control) PL spectra of IPA at different excitation wavelengths.

Supplementary Tauc analysis of MoS₂ QDs

As commented in the main text, the Tauc plot analysis of nanocrystals can be trivial and the E_g values of MoS₂ QDs calculated by Tauc analysis has to be considered qualitatively.²¹ Previous work suggested to correct the Tauc relation for direct-allowed transition in nanocrystals by assuming the power factor (n) equal to 1.²¹ **Figure S7** reports the Tauc plot for $n = 1$, which the E_g values to be estimated at ~ 3.2 eV.

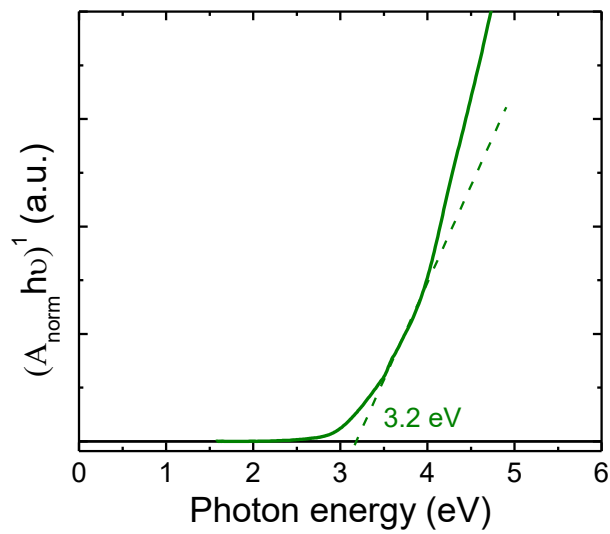


Figure S7. Tauc plot of MoS₂ QDs with $n = 1$.

Energy-dispersive X-ray spectroscopy of the MAPbI₃/MoS₂ QDs:f-RGO

Scanning electron microscopy combined with energy-dispersive X-ray spectroscopy (SEM/EDX) was carried out in order to gain insight into the coverage of the mesoscopic methylammonium lead iodide (CH₃NH₃PbI₃) perovskite (MAPbI₃) layer with MoS₂ QDs and f-RGO (**Figure S8a-c**) by preparing the perovskite solar cells (PSCs) as detailed in the Experimental Section (main text) up to the layer object of study. By analyzing the Pb (M, 2.34 keV), Mo (L α , 2.29 keV) and C (K α , 0.28 keV) peak signals by INCA[®] software (XPP matrix correction routine, which considers the atomic number and absorption effects for a standardless estimation of the composition), we confirmed the presence of MoS₂ QDs and f-RGO on the PSCs layer stack (**Figure S8d-h**). For the careful interpretation of the EDX data, it is important to note that (i) MAPbI₃ is already giving a C signal corresponding to the CH₃NH₃ and (ii) the Pb and Mo signals almost overlap making difficult to discern both components. Moreover, since the spiro-OMeTAD could also contribute to the C signal, we suppressed this layer in the preparation of the devices for these SEM/EDX measurements. As a control, we also determined the I/Pb atomic ratio (I (L α , 3.94 keV)) in all the samples. In this way, we obtained by evaluating at least 5 areas of about 12 \times 12 μ m² in two samples of each type of PSC values of C/Pb = 2.2 \pm 0.1 and I/Pb = 3.0 \pm 0.1 (for the reference MAPbI₃, **Figure S8d**); C/Pb = 16 \pm 2 and I/Pb = 3.0 \pm 0.1 (for f-RGO/MAPbI₃, **Figure S7e**); C/(Pb+Mo) = 2.3 \pm 0.2 and I/Pb = 3.0 \pm 0.1 (for MoS₂ QDs/MAPbI₃, **Figure S7f**) and C/(Pb+Mo) = 15 \pm 2 and I/Pb = 3.1 \pm 0.1 (for MoS₂ QDs:f-RGO/MAPbI₃, **Figure S8g-h**). These results show that the presence of f-RGO promotes the increase of the C/Pb ratio, while the I/Pb stoichiometry (3:1) of the perovskite is preserved.

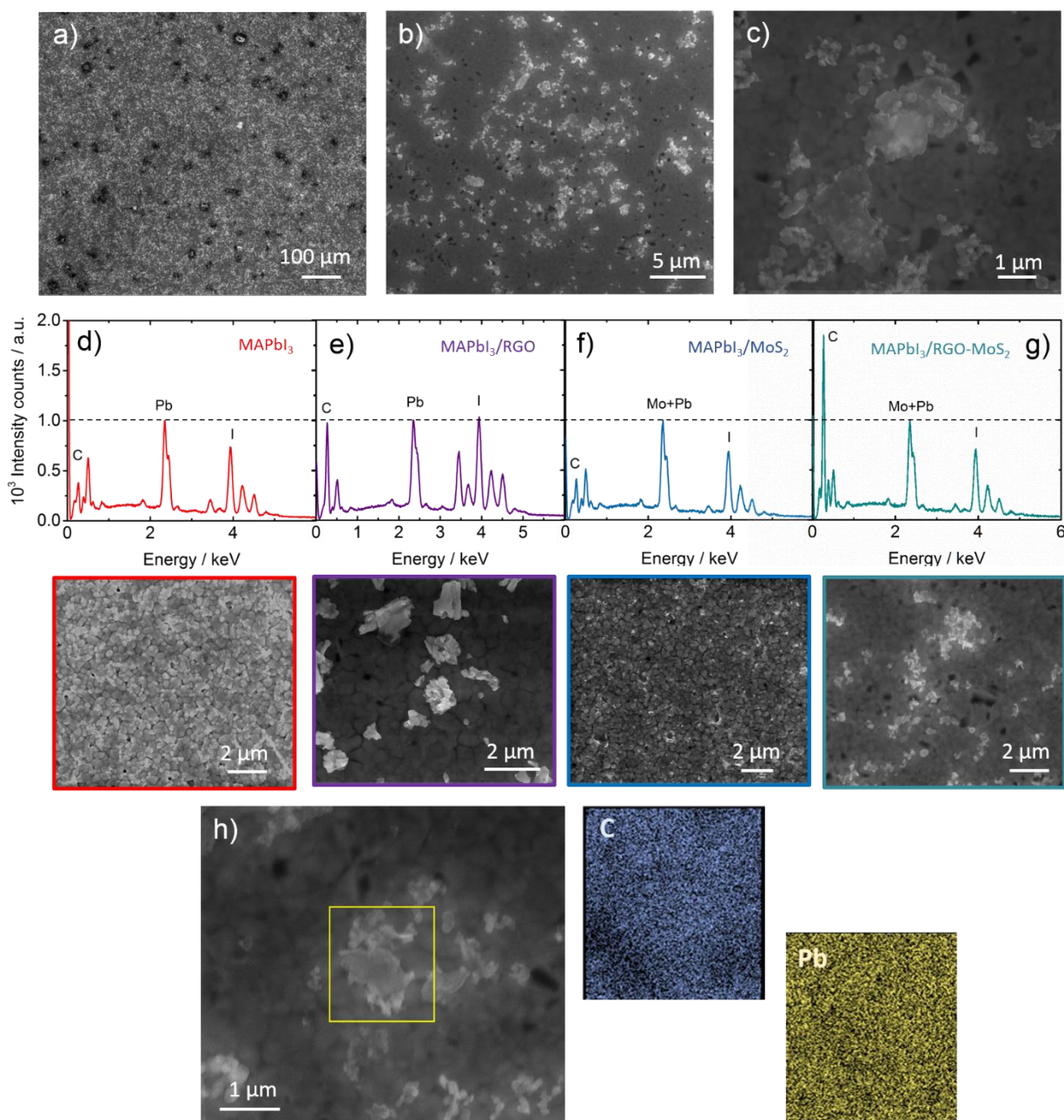


Figure S8. (a-c) Representative SEM images at different magnifications for the MoS₂ QDs:f-RGO/MAPbI₃ sample showing the coverage of the perovskite layer. Representative EDX spectra collected in areas of about 12x12 μm² for: (d) the reference MAPbI₃, (e) f-RGO/MAPbI₃, (f) MoS₂ QDs/MAPbI₃ and (g) MoS₂ QDs:f-RGO/MAPbI₃ normalized to the Pb signal accompanied of detailed SEM images. (h) A representative SEM/EDX mapping example for a small area (2x2 μm²) of MoS₂ QDs:f-RGO/MAPbI₃ sample pointed out in a yellow square.

Optical absorption spectroscopy measurements of PSCs

Figure S9 shows the UV-VIS absorption spectra of the different PSC architectures before the Au contact deposition. These results evidenced that the optical absorption of the MoS₂ QDs:f-RGO-based PSCs did not show significant differences compared to that of MoS₂ QDs-based PSC, and exhibited an increase by only ~3% and ~8% compared to that of f-RGO-based and reference PSCs. On the basis of these results, the enhanced J_{sc} value obtained with the use of f-RGO and MoS₂ QDs:f-RGO compared to that of reference device and the one of the device based on MoS₂ QDs can be attributed to the efficient charge collection in presence of f-RGO and MoS₂ QDs:f-RGO, respectively.

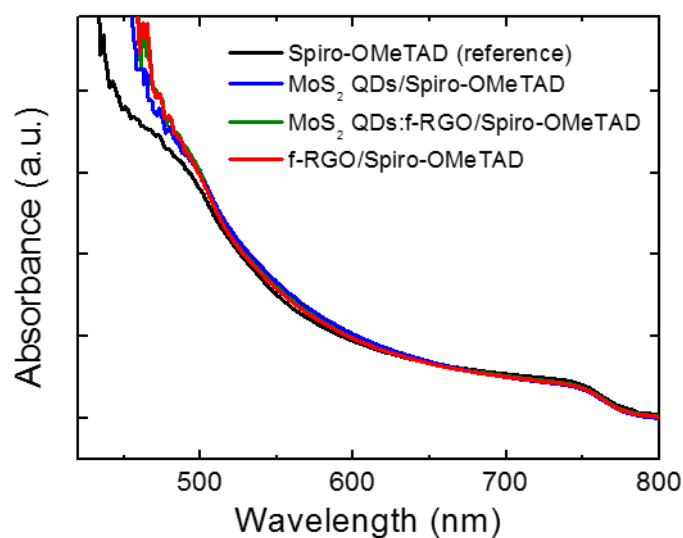


Figure S9. Absorption spectra of different PSCs before Au deposition.

Stabilized power conversion efficiency measurements

Figure S10 shows the stabilized power conversion efficiency (PCE) measurement performed with maximum power point (MPP) tracking on PSCs based on MoS₂ QDs, f-RGO and MoS₂ QDs:f-RGO as active buffer layer (ABL). The comparison with the measurement performed on reference ABL-free PSC based on solely spiro-OMeTAD as hole transport layer (HTL) is also shown. The results confirmed that the presence of MoS₂ QDs:f-RGO, as well as the f-RGO, enhance the performance of reference PSC. These results are in agreement with the I-V curve measurements of the various PSCs and the corresponding statistical analysis of the main PV parameters reported in the main text (Figure 5b and Figure 6, respectively).

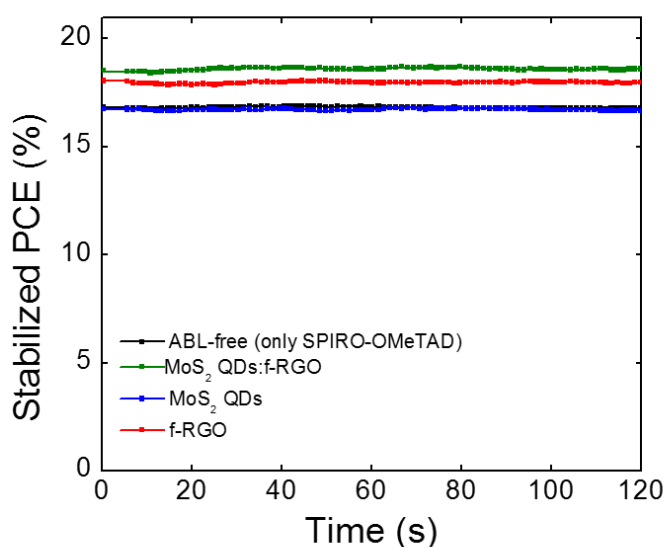


Figure S10. Stabilized PCE measurements performed with MPP tracking of the various PSCs based on MoS₂ QDs, f-RGO and MoS₂ QDs:f-RGO as ABL. The comparison with the measurement performed on reference ABL-free PSC based on exclusively spiro-OMeTAD as HTL is also shown

Hysteresis analysis

Figure S11 reports the forward and reverse I-V curves for the PSCs based MoS₂ QDs, f-RGO and MoS₂ QDs:f-RGO as ABLs. The comparison with the measurements performed on reference ABL-free PSC based on solely spiro-OMeTAD as HTL is also shown. Clearly, the presence of MoS₂ QDs:f-RGO as ABLs, in addition to increase the PCE, also decreases the hysteresis phenomena compared to those of reference PSCs and the other ABL-based devices.

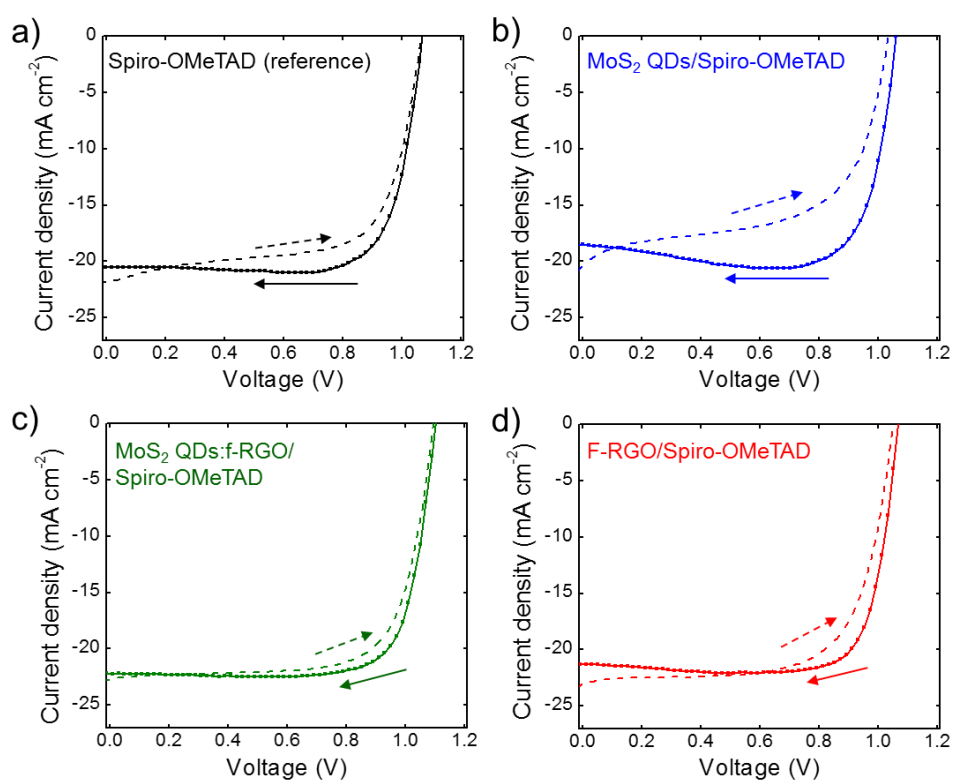


Figure S11. Forward and reverse I-V curves for the PSCs based on (a) solely spiro-OMeTAD (reference), (b) spiro-OMeTAD/MoS₂ QDs, (c) spiro-OMeTAD/MoS₂ QDs:f-RGO and (d) spiro-OMeTAD/f-RGO.

Spray coating parameter optimization for MoS₂ QDs, f-RGO and MoS₂ QDs:f-RGO film deposition

The spray coating deposition of MoS₂ QDs, f-RGO and MoS₂ QDs:f-RGO dispersion in IPA onto MAPbI₃ surface could degrade the native properties of the latter. In order to retain the optical properties of MAPbI₃, the spray coating was carried out by using N₂ as inert flowing gas, and the deposition parameters (N₂ pressure (P_{N2}), nozzle aperture (AP_{nozzle}), nozzle distance (d_{nozzle}), temperature of substrate (T_{sub}), spray velocity (v_{spray}), and flow rate of solution (FR_{solution})) were optimized by monitoring their influence on the UV-Vis absorption spectrum of MAPbI₃ substrates. The degradation of the perovskite was quantified by the relative optical absorption loss, *i.e.*, the module of ratio between the difference of its optical absorption before (Abs₀) and after (Abs_{spray}) material spray coating referred to Abs₀ (in formula: |(Abs₀-Abs_{spray})/Abs₀|).

Figure S12a shows the degradation (average values calculated in the ranges of 420-600 nm and 700-780 nm) measured by varying the most critical spray coating parameters and adopting d_{nozzle} = 9 cm, v_{spray} = 300mm s⁻¹, FR_{solution} = 20%. The best parameters were found to be: P_{N2} = 1 bar, AP_{nozzle} = 0.6 mm, d_{nozzle} = 9 cm, T_{sub} = 80 °C, v_{spray} = 300mm s⁻¹, and a FR_{solution} = 20%. The corresponding degradation of MAPbI₃ film was less than 2% (Figure S12b).

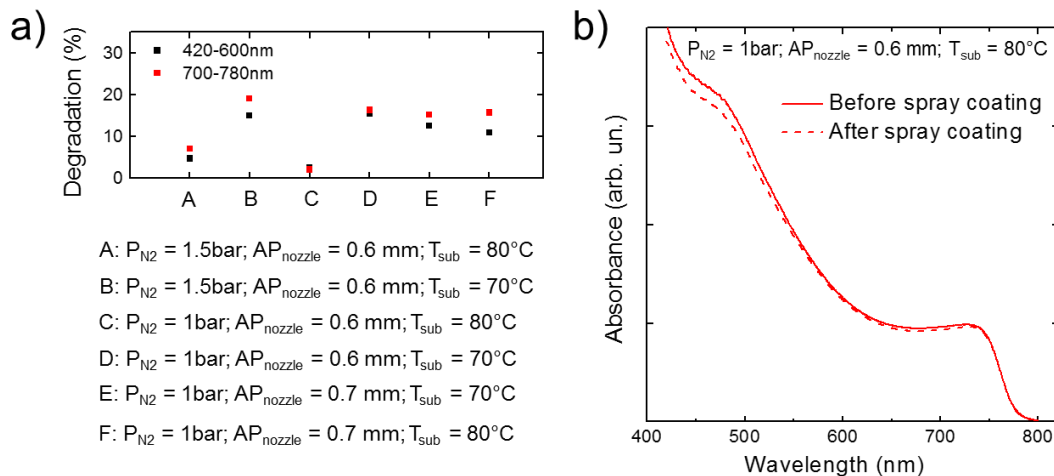


Figure S12. a) Sketch of the degradation of MAPbI₃ as a function of spray coating settings. b) Absorbance of MAPbI₃ before and after spray coating of IPA with optimized parameter setting denoted as C in panel a: P_{N₂} = 1 bar, A_{P_{nozzle}} = 0.6 mm, d_{nozzle} = 9 cm, T_{sub} = 80 °C, v_{spray} = 300mm s⁻¹, and a FR_{solution} = 20%.

REFERENCES

- (1) Mak, K. F.; Lee, C.; Hone, J.; Shan, J.; Heinz, T. F. Atomically Thin MoS₂: A New Direct-Gap Semiconductor. *Phys. Rev. Lett.* **2010**, *105* (13), 136805.
- (2) Lee, C.; Yan, H.; Brus, L. E.; Heinz, T. F.; Hone, J.; Ryu, S. Anomalous Lattice Vibrations of Single- and Few-Layer MoS₂. *ACS Nano* **2010**, *4* (5), 2695–2700.
- (3) Huang, Y.; Wu, J.; Hwang, K. C. Thickness of Graphene and Single-Wall Carbon Nanotubes. *Phys. Rev. B* **2006**, *74* (24), 245413.
- (4) Novoselov, K. S.; Geim, A. K.; Morozov, S. V.; Jiang, D.; Zhang, Y.; Dubonos, S. V.; Grigorieva, I. V.; Firsov, A. A. Electric Field Effect in Atomically Thin Carbon Films. *Science* **2004**, *306* (5696), 666–669.
- (5) Saito, R.; Tatsumi, Y.; Huang, S.; Ling, X.; Dresselhaus, M.S. Raman Spectroscopy of Transition Metal Dichalcogenides. *J. Phys. Condens. Matter* **2016**, *28* (35), 353002.
- (6) Bellani, S.; Najafi, L.; Capasso, A.; Del Rio Castillo, A. E.; Antognazza, M. R.; Bonaccorso, F. Few-Layer MoS₂ Flakes as a Hole-Selective Layer for Solution-Processed Hybrid Organic Hydrogen-Evolving Photocathodes. *J. Mater. Chem. A* **2017**, *5* (9), 4384–4396.
- (7) Ferrari, A. C.; Basko, D. M. Raman Spectroscopy as a Versatile Tool for Studying the Properties of Graphene. *Nat. Nanotechnol.* **2013**, *8*, 235.
- (8) Ferrari, A. C.; Meyer, J. C.; Scardaci, V.; Casiraghi, C.; Lazzeri, M.; Mauri, F.; Piscanec,

- S.; Jiang, D.; Novoselov, K. S.; Roth, S.; *et al.* Raman Spectrum of Graphene and Graphene Layers. *Phys. Rev. Lett.* **2006**, *97* (18), 187401.
- (9) Su, C.-Y.; Xu, Y.; Zhang, W.; Zhao, J.; Tang, X.; Tsai, C.-H.; Li, L.-J. Electrical and Spectroscopic Characterizations of Ultra-Large Reduced Graphene Oxide Monolayers. *Chem. Mater.* **2009**, *21* (23), 5674–5680.
- (10) Maragó, O. M.; Bonaccorso, F.; Saija, R.; Privitera, G.; Gucciardi, P. G.; Iati, M. A.; Calogero, G.; Jones, P. H.; Borghese, F.; Denti, P.; *et al.* Brownian Motion of Graphene. *ACS Nano* **2010**, *4* (12), 7515–7523.
- (11) Wang, P.; Liu, Z.-G.; Chen, X.; Meng, F.-L.; Liu, J.-H.; Huang, X.-J. UV Irradiation Synthesis of an Au–graphene Nanocomposite with Enhanced Electrochemical Sensing Properties. *J. Mater. Chem. A* **2013**, *1* (32), 9189–9195.
- (12) Hou, S.; Su, S.; Kasner, M. L.; Shah, P.; Patel, K.; Madarang, C. J. Formation of Highly Stable Dispersions of Silane-Functionalized Reduced Graphene Oxide. *Chem. Phys. Lett.* **2010**, *501* (1), 68–74.
- (13) Yao, H.; Jin, L.; Sue, H.-J.; Sumi, Y.; Nishimura, R. Facile Decoration of Au Nanoparticles on Reduced Graphene Oxide Surfaces *via* a One-Step Chemical Functionalization Approach. *J. Mater. Chem. A* **2013**, *1* (36), 10783.
- (14) Martin-Garcia, B.; Polovitsyn, A.; Prato, M.; Moreels, I. Efficient Charge Transfer in Solution-Processed PbS Quantum Dot-Reduced Graphene Oxide Hybrid Materials. *J. Mater. Chem. C* **2015**, *3* (27), 7088–7095.

- (15) Villa, S.; Riani, P.; Locardi, F.; Canepa, F. Functionalization of Fe₃O₄ NPs by Silanization: Use of Amine (APTES) and Thiol (MPTMS) Silanes and Their Physical Characterization. *Materials (Basel)*. **2016**, *9* (10), 826.
- (16) Willis, L. J.; Loehr, T. M.; Miller, K. F.; Bruce, A. E.; Stiefel, E. I. Raman and Infrared Spectroscopic Studies of Dioxomolybdenum(VI) Complexes with Cysteamine Chelates. *Inorg. Chem.* **1986**, *25* (23), 4289–4293.
- (17) Nagaraju, G.; Tharamani, C. N.; Chandrappa, G. T.; Livage, J. Hydrothermal Synthesis of Amorphous MoS₂ Nanofiber Bundles *via* Acidification of Ammonium Heptamolybdate Tetrahydrate. *Nanoscale Res. Lett.* **2007**, *2* (9), 461–468.
- (18) Gan, Z. X.; Liu, L. Z.; Wu, H. Y.; Hao, Y. L.; Shan, Y.; Wu, X. L.; Chu, P. K. Quantum Confinement Effects across Two-Dimensional Planes in MoS₂ Quantum Dots. *Appl. Phys. Lett.* **2015**, *106* (23), 233113.
- (19) Gan, Z.; Xu, H.; Hao, Y. Mechanism for Excitation-Dependent Photoluminescence from Graphene Quantum Dots and Other Graphene Oxide Derivates: Consensus, Debates and Challenges. *Nanoscale* **2016**, *8* (15), 7794–7807.
- (20) Gopalakrishnan, D.; Damien, D.; Li, B.; Gullappalli, H.; Pillai, V. K.; Ajayan, P. M.; Shaijumon, M. M. Electrochemical Synthesis of Luminescent MoS₂ Quantum Dots. *Chem. Commun.* **2015**, *51* (29), 6293–6296.
- (21) Feng, Y.; Lin, S.; Huang, S.; Shrestha, S.; Conibeer, G. Can Tauc Plot Extrapolation Be Used for Direct-Band-Gap Semiconductor Nanocrystals? *J. Appl. Phys.* **2015**, *117* (12), 125701.